

**ELECTROOPTIC MATCHED FILTER CONTROLLED BY INDEPENDENT
VOLTAGES APPLIED TO MULTIPLE SETS OF ELECTRODES**

A Thesis

by

CHANGDONG KIM

Submitted to the Office of Graduate Studies of
Texas A&M University
in partial fulfillment of the requirements for the degree of

MASTER OF SCIENCE

December 2005

Major Subject: Electrical Engineering

**ELECTROOPTIC MATCHED FILTER CONTROLLED BY INDEPENDENT
VOLTAGES APPLIED TO MULTIPLE SETS OF ELECTRODES**

A Thesis

by

CHANGDONG KIM

Submitted to the Office of Graduate Studies of
Texas A&M University
in partial fulfillment of the requirements for the degree of

MASTER OF SCIENCE

Approved by:

Chair of Committee,	Henry F. Taylor
Committee Members,	Ohannes Eknayan
	Krzysztof A. Michalski
	Alexei V. Sokolov
Head of Department,	Chanan Singh

December 2005

Major Subject: Electrical Engineering

ABSTRACT

Electrooptic Matched Filter Controlled by Independent Voltages Applied to Multiple Sets of Electrodes. (December 2005)

Changdong Kim, B.S., Korea University

Chair of Advisory Committee: Dr. Henry F. Taylor

Analysis and experimental results on a polarization independent electrooptic matched filter (EMF) with a center wavelength of 1.53 μm are reported. The EMF utilizes electrooptic phase-matched TE \leftrightarrow TM conversion in a Ti-diffused waveguide on a LiNbO₃ substrate. The operation of the EMF to select an optical frequency channel is controlled by applying independent voltages to interdigital electrode sets cascaded along a single mode waveguide. The device is inherently polarization independent and has the potential for submicrosecond tuning. The number of selectable channels N is related to the number of electrode sets P by the formula $N = P / 2 + 1$. A matrix analysis is used to determine the TE \leftrightarrow TM conversion efficiency for the case that $P = 8$ and $N = 5$. A driving circuit for the EMF was implemented using a digital-to-analog converter (DAC) array controlled from a personal computer (PC). Transmittance spectra of a filter produced in a LiNbO₃ substrate are presented. A raised cosine weighting function applied along the 3.8 cm length of an EMF provides a sidelobe suppression level better than -17 dB with a 1.0 nm 3-dB bandwidth.

To My Mother, Ieboon Im

ACKNOWLEDGEMENTS

I am grateful to my advisor, Dr. Henry F. Taylor who has provided guidance and support in academic endeavors for this research. I am also very appreciative of the support of my academic development by Dr. Ohannes Eknayan. In addition, I would like to thank my committee members, Dr. Krzysztof A. Michalski and Dr. Alexei V. Sokolov and the laboratory coordinator, Mr. Robert Atkins, for their efforts to facilitate everything. I am particularly thankful to Yang Ping for the fabricating devices and for sharing his experience in our test. Thanks also to Taehan Bae and Yongwook Shin for their support and guidance throughout my graduate education.

I also wish to express my gratitude to everyone outside of Zachry Engineering Center. Their friendship and help have played an important role in the completion of my education at Texas A&M University. Finally, I would like to thank my family who have always encouraged me in every way.

TABLE OF CONTENTS

	Page
ABSTRACT	iii
DEDICATION	iv
ACKNOWLEDGEMENTS	v
TABLE OF CONTENTS	vi
LIST OF FIGURES	viii
LIST OF TABLES	x
 CHAPTER	
I INTRODUCTION.....	1
II MODE COUPLING IN OPTICAL WAVEGUIDE	4
A. TE and TM Modes in Slab Dielectric Waveguide	4
1. Wave Equation in Slab Waveguide.....	4
2. TE Modes	5
3. TM Modes.....	7
B. TE/TM Polarization Converter	8
1. Coupled Mode Theory in Optical Waveguide	8
2. Electrooptic Effect in a Uniaxial Crystal	11
3. TE↔TM Mode Converter.....	16
III DESIGN OF ELECTROOPTIC MATCHED FILTER	19
A. The Principal Characteristics of EMF	19
B. The EMF Structure for Two Sidebands.....	21
C. The EMF Structure for Single Sideband	24
D. Matrix Formulation and Simulation Results	27
IV ELECTRONIC DRIVING CIRCUIT FOR EMF	33
A. Digital-to-Analog Converter Driving Circuit.....	33
B. Loading DAC Channels.....	34
V EXPERIMENTAL RESULTS	36
A. Experimental Configuration	36

CHAPTER	Page
B. Test Results.....	36
VI CONCLUSIONS.....	41
VII RECOMMENDATIONS	43
REFERENCES.....	45
APPENDIX A MATLAB CODE	47
APPENDIX B OP-AMP CIRCUIT	54
VITA	55

LIST OF FIGURES

FIGURE	Page
1 EOTF design in LiTaO ₃	2
2 Optical waveguide structures	4
3 Slab dielectric waveguide	5
4 The index ellipsoid for a uniaxial crystal.....	12
5 Principal axis rotation in a y-cut, x-propagating LiNbO ₃	14
6 Power transfer between two coupled optical waves	17
7 Periodic electrode structure for electrooptically induced TE-TM coupling.....	18
8 Cross-sectional view of electrodes.....	19
9 Schematic diagram of the EMF structure and orientation for two sidebands	22
10 Selection of voltages in the structure of two sidebands	23
11 Modified configuration in the series of electrodes for a single sideband	25
12 Selection of voltages in the structure of a single sideband	26
13 Simulated performances in the structure of two sidebands.....	30
14 Simulated performances in the single sideband configuration for channel -2.....	31
15 AD5379 board.....	33
16 Electronic driving circuit setup	34
17 Load DAC channels	34
18 A schematic diagram of experimental setup	36
19 The optical output power spectra of EMF for TE →TM polarization conversion in the structure for two sidebands.....	37

FIGURE	Page
20 EMF filter characteristic at channel 0	39
21 EMF filter characteristic at channel ± 1	40
22 EMF filter characteristic at channel ± 2	40

LIST OF TABLES

TABLE	Page
1 The ratio of V_{jp} applied to p'th channel to V_0 for the selection of j'th frequency channel in the structure of two sidebands	24
2 The ratio of V_{jp} applied to p'th channel to V_0 for the selection of j'th frequency channel in the structure of single sideband	27
3 14-bit data word format.....	35

CHAPTER I

INTRODUCTION

Optical filters are essential components in wavelength-division multiplexed (WDM) optical networks [1]. Communications has evolved from point to point transmission to multiplexed networks [2], and next-generation network functionality will be enhanced by reconfigurable optical add/drop multiplexers (ROADMs) [3]. These dynamic tunable optical filters are still at an early stage of development.

Among different technologies used to implement tunable optical filters, electrooptic tunable filters (EOTFs) provide a good solution for sub-microsecond tunability through TE-TM mode coupling [4]. A polarization-independent EOTF demonstrated in LiNbO₃ employed two identical TE↔TM polarization converters and TE/TM polarization splitters [5]. Another scheme in Fig. 1 using strain-induced polarization conversion in LiTaO₃ was also demonstrated [6]. These conventional EOTF designs utilize a Mach-Zehnder interferometer structure, phase-matched polarization conversion, and polarization beam splitters.

The primary objective of the research is to demonstrate the electrooptic matched filter (EMF), a new type of EOTF which provides wide spectral tuning range and rapid tuning. The EMF is designed for operation in the 1550 nm wavelength regime for 100 GHz (0.8 nm) channel spacing corresponding to the International Telecommunication Union – Telecommunication Standardization Sector (ITU-T) grid.

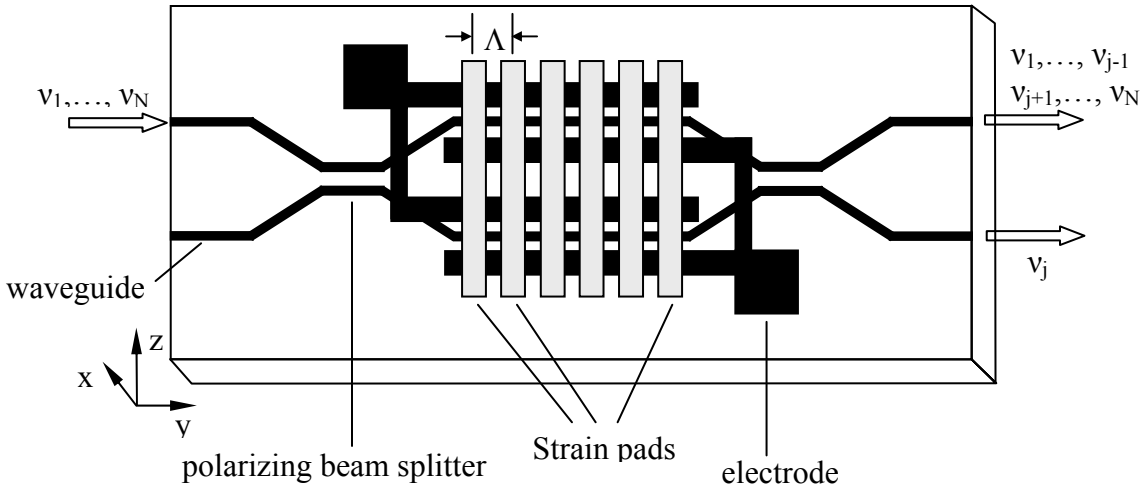


Fig. 1. EOTF design in LiTaO_3

The following features of EMF are expected from the results of this research:

- Spectral tuning range of 3.2 nm
- Submicrosecond tuning speed
- Single chip integration on a LiNbO_3 substrate
- Polarization independence
- High sidelobe suppression via raised-cosine apodization

Chapter II provides a description of fundamentals of polarization mode coupling in optical waveguides, which is the basis for operation of the EMF. Chapter III introduces the EMF structure and a matrix formulation to analyze $\text{TE} \leftrightarrow \text{TM}$ mode conversion and phase retardation quantitatively. Chapter IV describes the electronic circuitry developed to drive the EMF as required for selecting WDM channels. Measured spectral characteristics for an EMF produced on a LiNbO_3 substrate are presented in Chapter V, and the experimental results are compared with theory. Finally, conclusions

and recommendations for the future research work are presented in Chapters VI and VII.

CHAPTER II

MODE COUPLING IN OPTICAL WAVEGUIDE

A. TE and TM Modes in Slab Dielectric Waveguide

An optical waveguide is a medium of high refractive index surrounded by a dielectric material of lower refractive index to confine and direct the light. The structure of optical waveguides can be a slab (or planar), strip, or cylinder (Fig. 2). The optical fiber is a good example of a cylindrical waveguide. In this chapter, TE and TM modes for the general asymmetric slab dielectric waveguide and their coupling are described.

1. Wave Equation in Slab Waveguide

The step-index planar waveguide is the simplest structure for discussing fundamental properties of guided modes. The guiding layer (region II) has a higher refractive index than cover (region I) and the substrate (region III) as shown in Fig. 3, where the refractive indices of region I, II, and III are n_1 , n_2 , and n_3 , respectively. It is assumed that $n_2 > n_3 > n_1$. The allowed modes of this waveguide are obtained from

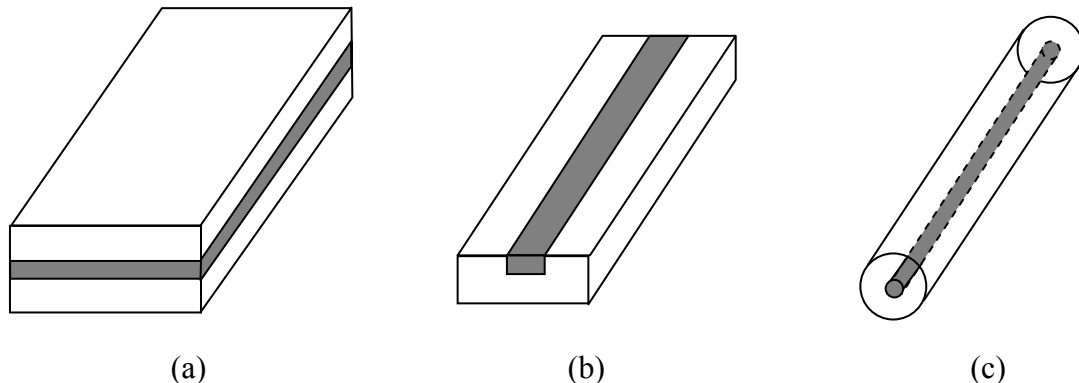


Fig. 2. Optical waveguide structures. (a) slab (b) strip and (c) fiber

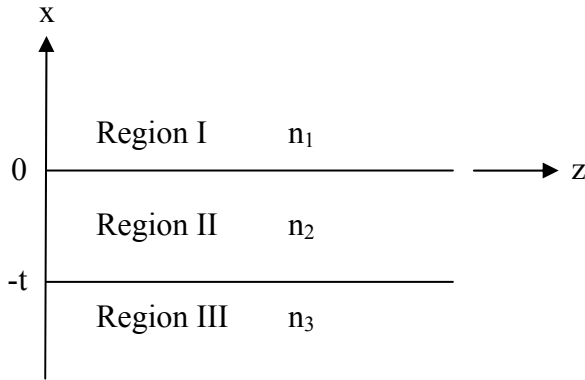


Fig. 3. Slab dielectric waveguide

the wave equation given by

$$\nabla^2 \mathbf{E}(\mathbf{r}) + k_0^2 n^2(\mathbf{r}) \mathbf{E}(\mathbf{r}) = 0 \quad (1)$$

where $k_0 \equiv \omega/c$ and n is the refractive index. The solutions are subject to the boundary conditions that tangential components of \mathbf{E} and \mathbf{H} are continuous at the interfaces $x = 0$ and $x = -t$. For the field propagating along the z-axis given by

$$\mathbf{E}(\mathbf{r}, t) = \mathbf{E}(x, y) e^{i(\omega t - \beta z)} \quad (2)$$

in infinite slab waveguides, where the electromagnetic fields are independent of y, equation 1 becomes

$$\frac{\partial^2}{\partial x^2} \mathbf{E}(x, y) + (k_0^2 n^2 - \beta^2) \mathbf{E}(x, y) = 0 \quad (3)$$

Here, ω is the frequency of the wave and β is the propagation constant.

2. TE Modes

Assuming an isotropic and lossless medium in the waveguide of Fig. 3, Maxwell's equations given by

$$\nabla \times \mathbf{E} = -\mu_0 \frac{\partial \mathbf{H}}{\partial t} \quad (4)$$

and

$$\nabla \times \mathbf{H} = -\epsilon_0 n^2 \frac{\partial \mathbf{E}}{\partial t} \quad (5)$$

yield two orthogonal modes: transverse electric (TE) mode and transverse magnetic (TM) mode [7]. The wave equation and Maxwell's equations for the TE mode are

$$\frac{\partial^2}{\partial x^2} E_y + (k_0^2 n^2 - \beta^2) E_y = 0 \quad (6)$$

$$H_y = -\frac{\beta}{\omega \mu_0} E_y \quad (7)$$

$$H_z = -\frac{1}{j \omega \mu_0} \frac{\partial E_y}{\partial x} \quad (8)$$

From equation 6 and boundary conditions in each layer, TE modes can be written as

$$\begin{aligned} E_y &= C e^{-qx}, x > 0 \\ E_y &= C [\cos(hx) - \frac{q}{h} \sin(hx)], -t \leq x \leq 0 \\ E_y &= C [\cos(ht) + \frac{q}{h} \sin(ht)] e^{p(x+t)}, x < -t \end{aligned} \quad (9)$$

where

$$q = \sqrt{\beta^2 - k_0^2 n_1^2}, h = \sqrt{k_0^2 n_2^2 - \beta^2}, p = \sqrt{\beta^2 - k_0^2 n_3^2} \quad (10)$$

and C is an arbitrary constant.

In the above discussion, the propagating constant β is $k_0 n_3 < \beta < k_0 n_2$ to support confined modes in the guiding layer. The eigenvalue equation written by

$$\tan(ht) = \frac{p+q}{h - \frac{pq}{h}} \quad (11)$$

is obtained from boundary condition of H_z at the interfaces $x=0$ and $x=-t$. Only discrete values of β satisfy equation 11 and are called eigenvalues for the guided TE modes.

3. TM Modes

TM modes are solution of the wave equation, given by

$$\frac{\partial^2}{\partial x^2} H_y + (k_0^2 n^2 - \beta^2) H_y = 0 \quad (12)$$

Maxwell's equations for the TM modes are

$$E_x = \frac{\beta}{\omega \epsilon_0 n^2} H_y \quad (13)$$

$$E_z = \frac{1}{j \omega \epsilon_0 n^2} \frac{\partial H_y}{\partial x} \quad (14)$$

The similar analysis to TE mode yields TM mode field solutions in the following:

$$\begin{aligned} H_y &= -C' \frac{h}{q} e^{-qx}, \quad x > 0 \\ H_y &= C' \left[-\frac{h}{q} \cos(hx) + \sin(hx) \right], \quad -t \leq x \leq 0 \\ H_y &= -C' \left[\frac{h}{q} \cos(ht) + \sin(ht) \right] e^{p(x+t)}, \quad x < -t \end{aligned} \quad (15)$$

where q , h , and p are same as equation 10 and the constant C' is chosen arbitrarily. Equation 15 and boundary conditions at the interfaces result in eigenvalue equation for TM modes given by

$$\tan(ht) = \frac{\frac{n_2^2}{n_3^2} p + \frac{n_2^2}{n_1^2} q}{h - \left(\frac{n_2^2}{n_1 n_3}\right)^2 \frac{pq}{h}} \quad (16)$$

B. TE/TM Polarization Converter

TE/TM polarization coupling, a key aspect of the EMF design, is described in this section. TE and TM polarizations experience polarization perturbation induced by refractive index changes in the waveguide through an applied electric field. General coupled mode formulation, the electrooptic effect in LiNbO₃ and the field solutions for TE and TM coupled mode equations are detailed in the following sections 1, 2, and 3, respectively.

1. Coupled Mode Theory in Optical Waveguide

In an isotropic charge-free medium, eigen modes in equations 9 and 15 satisfy the wave equation in the form

$$\nabla^2 \mathbf{E}(\mathbf{r}, t) = \mu \epsilon(\mathbf{r}) \frac{\partial^2 \mathbf{E}(\mathbf{r}, t)}{\partial t^2} \quad (17)$$

which is obtained from substituting the curl of equation 4 into equation 5 and using $\nabla \cdot (\epsilon \mathbf{E}) = 0$ and $\nabla \times \nabla \times \mathbf{E} \equiv \nabla(\nabla \cdot \mathbf{E}) - \nabla^2 \mathbf{E}$. With the electric polarization of the medium $\mathbf{P}(\mathbf{r}, t)$, equation 17 can be written as

$$\nabla^2 \mathbf{E}(\mathbf{r}, t) = \mu \epsilon_0 \frac{\partial^2 \mathbf{E}(\mathbf{r}, t)}{\partial t^2} + \mu \frac{\partial^2}{\partial t^2} \mathbf{P}(\mathbf{r}, t) \quad (18)$$

where $\mathbf{P}(\mathbf{r}, t) = [\epsilon(\mathbf{r}) - \epsilon_0] \mathbf{E}(\mathbf{r}, t)$ and $\epsilon(\mathbf{r})$ is the medium dielectric constant. If the deformation in the waveguide is taken into account, the induced perturbation in the polarization results in

$$\nabla^2 \mathbf{E}(\mathbf{r}, t) = \mu \frac{\partial^2}{\partial t^2} [\epsilon(\mathbf{r}) \mathbf{E}(\mathbf{r}, t) + \mathbf{P}_{pert}(\mathbf{r}, t)] \quad (19)$$

Assuming only the TE mode here because the same expression is made for other polarizations, the equation 19 becomes again

$$\nabla^2 E_y(\mathbf{r}, t) - \mu \frac{\partial^2}{\partial t^2} \epsilon(\mathbf{r}) E_y(\mathbf{r}, t) = \mu \frac{\partial^2}{\partial t^2} [P_{pert}(\mathbf{r}, t)]_y \quad (20)$$

The solutions of equation 20 are obtained in two steps: first, we ignore the perturbation term on the right-hand side of equation 20 and find the solution in unperturbed waveguide. Then, we substitute it into equation 20 and get a final solution of the perturbed waveguide with some assumptions. The solution for the unperturbed waveguide of Fig. 3 is

$$E_y(\mathbf{r}, t) = \frac{1}{2} \sum_m A_m E_y^m(x) e^{j(\omega t - \beta_m z)} + c.c. \quad (21)$$

where m implies the m th eigenmode, A_m is the amplitude, and $E_y^m(x)$ is the transverse distribution. It is noted that $E_y^m(x)$ satisfies equation 20 without the perturbation term in the right-hand side so that

$$\left(\frac{d^2}{dx^2} - \beta_m^2 \right) E_y^m(x) + \omega^2 \mu \epsilon(\mathbf{r}) E_y^m(x) = 0 \quad (22)$$

Assuming small deformation, only A_m is changed to $A_m(z)$. Substituting equation 21 into equation 20, we have

$$e^{j\omega t} \sum_m \left[\frac{A_m}{2} \left(\frac{d^2}{dx^2} - \beta_m^2 + \omega^2 \mu \epsilon(\mathbf{r}) \right) E_y^m(x) e^{-j\beta_m z} \right. \\ \left. + \frac{1}{2} \left(\frac{d^2 A_m}{dz^2} - 2j\beta_m \frac{dA_m}{dz} \right) E_y^m(x) e^{-j\beta_m z} \right] + c.c. = \mu \frac{\partial^2}{\partial t^2} [P_{pert}(\mathbf{r}, t)]_y \quad (23)$$

From equation 22 and $\frac{d^2 A_m}{dz^2} \ll \beta_m \frac{dA_m}{dz}$ where small variation in A_m is assumed,

equation 23 is written as

$$\sum_m -j\beta_m \frac{dA_m}{dz} E_y^m(x) e^{-j(\omega t - \beta_m z)} + c.c. = \mu \frac{\partial^2}{\partial t^2} [P_{pert}(\mathbf{r}, t)]_y \quad (24)$$

We multiply equation 24 by the s th eigenmode $E_y^s(x)$ and integrate with respect to x .

From the orthogonality between modes given by $\int_{-\infty}^{\infty} E_y^m(x) E_y^s(x) dx = \frac{2\omega\mu}{\beta_s} \delta_{sm}$ with

$\delta_{sm} = -1$ if $s = m$ and $\delta_{sm} = 0$ otherwise, the following expression is derived:

$$\frac{dA_s^-}{dz} e^{j(\omega t + \beta_s z)} - \frac{dA_s^+}{dz} e^{j(\omega t - \beta_s z)} - c.c. = -\frac{j}{2\omega} \frac{\partial^2}{\partial t^2} \int_{-\infty}^{\infty} [P_{pert}(\mathbf{r}, t)]_y E_y^s(x) dx \quad (25)$$

In the left-hand side of equation 25, two waves propagating forward (to the $+z$ side) and backward (to the $-z$ side) are included. This equation is used to consider TE and TM mode interaction.

2. Electrooptic Effect in a Uniaxial Crystal

An electrooptic material undergoes the change in the refractive index induced by applied electric field linearly (Pockels effect) or quadratically (Kerr effect) and this phenomenon is called the electrooptic effect [8]. The electrooptic effect is used for optical phase modulation and phase retardation to fabricate electrically controllable optical devices. This section starts with a brief description of anisotropic media including LiNbO₃.

The electric flux density \mathbf{D} in an anisotropic dielectric media is written by with dielectric constants and electric fields

$$\begin{aligned} D_x &= \epsilon_{11}E_x + \epsilon_{12}E_y + \epsilon_{13}E_z \\ D_y &= \epsilon_{21}E_x + \epsilon_{22}E_y + \epsilon_{23}E_z \\ D_z &= \epsilon_{31}E_x + \epsilon_{32}E_y + \epsilon_{33}E_z \end{aligned} \quad (26)$$

If the coordinate system in a crystal structure is chosen to vanish off-diagonal elements, the axes in this coordinate system are defined as principal axes and a 3×3 electric permeability tensor can be expressed as

$$[\epsilon] = \begin{bmatrix} \epsilon_{11} & 0 & 0 \\ 0 & \epsilon_{22} & 0 \\ 0 & 0 & \epsilon_{33} \end{bmatrix} \quad (27)$$

Recalling the electric energy density stored in a crystal $w_e = \frac{1}{2}\mathbf{E} \cdot \mathbf{D}$ and $\mathbf{D} = \epsilon_0[\epsilon]\mathbf{E}$, w_e takes a form of

$$w_e = \frac{1}{2} \left(\frac{D_x^2}{\epsilon_{11}} + \frac{D_y^2}{\epsilon_{22}} + \frac{D_z^2}{\epsilon_{33}} \right) \quad (28)$$

Replacing $D_i / \sqrt{2\epsilon_0 w_e}$ where $i = x, y, z$ and ϵ_0 is the electric permeability of free space with X, Y , and Z in equation 28, we have the index ellipsoid described by

$$\frac{X^2}{n_x^2} + \frac{Y^2}{n_y^2} + \frac{Z^2}{n_z^2} = 1 \quad (29)$$

where $n_x = \sqrt{\epsilon_{11}/\epsilon_0}$, $n_y = \sqrt{\epsilon_{22}/\epsilon_0}$ and $n_z = \sqrt{\epsilon_{33}/\epsilon_0}$ are principal refractive indices.

Equation 29 delineates the optical properties of anisotropic media in a complete manner. An isotropic crystal characterized by $n_x = n_y = n_z$ has a spherical index ellipsoid. A uniaxial media takes the ellipsoid of revolution as the shape of index ellipsoid since $n_x = n_y \neq n_z$. In the uniaxial crystal, it is noticed that $n_x = n_y = n_o$ and $n_z = n_e$ where n_o and n_e are called the ordinary and extraordinary indices, respectively and the z axis is called the optic axis (Fig. 4).

The presence of electric field applied in an arbitrary direction to a crystal leads to a linear change in the coefficient $1/n_i^2$ according to

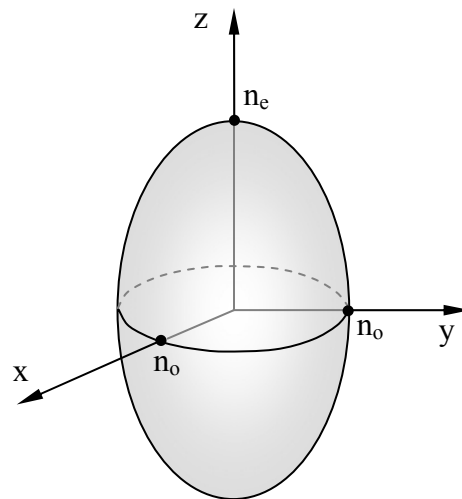


Fig. 4. The index ellipsoid for a uniaxial crystal

$$\Delta\left(\frac{1}{n^2}\right)_i = \sum_j r_{ij} E_j \quad i=1, \dots, 6, \quad j=1, 2, 3 \quad (30)$$

In a matrix form, equation 30 is written by

$$\begin{vmatrix} \Delta(1/n^2)_1 \\ \Delta(1/n^2)_2 \\ \Delta(1/n^2)_3 \\ \Delta(1/n^2)_4 \\ \Delta(1/n^2)_5 \\ \Delta(1/n^2)_6 \end{vmatrix} = \begin{vmatrix} r_{11} & r_{12} & r_{13} \\ r_{21} & r_{22} & r_{23} \\ r_{31} & r_{32} & r_{33} \\ r_{41} & r_{42} & r_{43} \\ r_{51} & r_{52} & r_{53} \\ r_{61} & r_{62} & r_{63} \end{vmatrix} \begin{vmatrix} E_1 \\ E_2 \\ E_3 \end{vmatrix} \quad (31)$$

The 6×3 electrooptic tensor composed of the electrooptic coefficient r_{ij} has a different form for noncentroelectric crystals. The electrooptic tensor of LiNbO₃ which is a uniaxial material of the 3m trigonal crystal class [9] is given by

$$\begin{bmatrix} 0 & -r_{22} & r_{13} \\ 0 & r_{22} & r_{13} \\ 0 & 0 & r_{33} \\ 0 & r_{51} & 0 \\ r_{51} & 0 & 0 \\ -r_{22} & 0 & 0 \end{bmatrix} \quad (32)$$

The new index ellipsoid in the applied electric field is described by

$$\left(\frac{1}{n^2}\right)_1' x^2 + \left(\frac{1}{n^2}\right)_2' y^2 + \left(\frac{1}{n^2}\right)_3' z^2 + 2\left(\frac{1}{n^2}\right)_4' yz + 2\left(\frac{1}{n^2}\right)_5' xz + 2\left(\frac{1}{n^2}\right)_6' xy = 1 \quad (33)$$

where the impermeability tensor is no longer diagonal such as below

$$[1/n^2]' = \begin{bmatrix} 1/n_x^2 + \Delta(1/n^2)_1 & \Delta(1/n^2)_6 & \Delta(1/n^2)_5 \\ \Delta(1/n^2)_6 & 1/n_y^2 + \Delta(1/n^2)_2 & \Delta(1/n^2)_4 \\ \Delta(1/n^2)_5 & \Delta(1/n^2)_4 & 1/n_z^2 + \Delta(1/n^2)_3 \end{bmatrix} \quad (34)$$

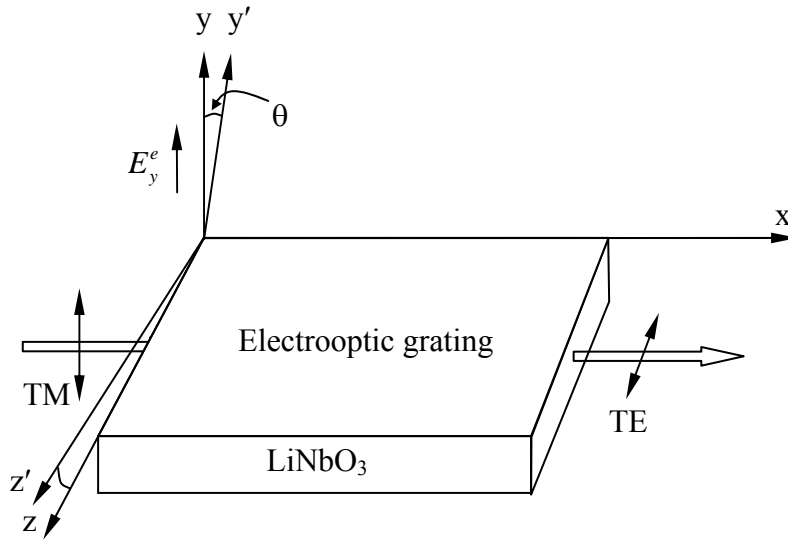


Fig. 5. Principal axis rotation in a y-cut, x-propagating LiNbO_3

For various electric field directions in y-cut, x-propagating LiNbO_3 , the electric field E_y^e applied uniformly along y axis is considered in Fig. 5. When the electric field E_y^e is applied, the index ellipsoid becomes

$$\left(\frac{1}{n_o^2} + r_{22} E_y^e \right) y^2 + \left(\frac{1}{n_e^2} \right) z^2 + 2r_{51} E_y^e yz = 1 \quad (35)$$

In equation 35, the existence of the mixed yz term implies the index ellipsoid is rotated about x axis and x, y, and z are no longer the principal axes. The perturbed index ellipsoid in new $x'y'$ plane is expressed by

$$\frac{y'^2}{n_{y'}^2} + \frac{z'^2}{n_{z'}^2} = 1 \quad (36)$$

where the new principal axes x , y' , and z' can be written as

$$\begin{bmatrix} x \\ y' \\ z' \end{bmatrix} = [T] \begin{bmatrix} x \\ y \\ z \end{bmatrix}, \quad [T] = \begin{bmatrix} 1 & 0 & 0 \\ 0 & \cos\theta & -\sin\theta \\ 0 & \sin\theta & \cos\theta \end{bmatrix} \quad (37)$$

Substituting equation 37 into equation 36 and comparing to equation 35, the rotation θ about x axis is described by

$$\tan 2\theta = \frac{2r_{51}E_y^e}{1/n_e^2 - 1/n_o^2} \quad (38)$$

The refractive indices $n_{x'}$, $n_{y'}$ and $n_{z'}$ are found as [10]

$$\begin{aligned} n_{x'} &= n_o + \frac{1}{2}n_o^3 r_{22} E_y^e \\ n_{y'} &= n_o - \frac{1}{2}n_o^3 r_{22} E_y^e + \frac{n_o^3(r_{51}E_y^e)^2}{1/n_e^2 - 1/n_o^2} \\ n_{z'} &= n_e - \frac{n_e^3(r_{51}E_y^e)^2}{1/n_e^2 - 1/n_o^2} \end{aligned} \quad (39)$$

Since practically $n_{x'} \approx n_o$, $n_{y'} \approx n_o$, and $n_{z'} \approx n_e$ for LiNbO₃,

$$[\varepsilon'] = \begin{bmatrix} n_{x'}^2 & 0 & 0 \\ 0 & n_{y'}^2 & 0 \\ 0 & 0 & n_{z'}^2 \end{bmatrix} \approx \begin{bmatrix} n_o^2 & 0 & 0 \\ 0 & n_o^2 & 0 \\ 0 & 0 & n_e^2 \end{bmatrix} \quad (40)$$

The permeability tensor $[\varepsilon]$ in the x , y , and z coordinate system becomes diagonal form according to the transformation $[\varepsilon] = [T]^T [\varepsilon'] [T]$ and written by

$$[\varepsilon] = \begin{bmatrix} \varepsilon_{11} & 0 & 0 \\ 0 & \varepsilon_{22} & \delta\varepsilon_{23} \\ 0 & \delta\varepsilon_{23} & \varepsilon_{33} \end{bmatrix} \quad (41)$$

where $\delta\varepsilon_{23} = -n_e^2 n_o^2 r_{51} E_y^e$. Considering the TM polarized optical wave E_y^ω propagates in a crystal and off-diagonal elements in the permeability tensor are induced by electric field E_y^e , the polarization $\delta\mathbf{P} = \varepsilon_0([\varepsilon'] - [\varepsilon])\mathbf{E}$ is described by

$$\begin{bmatrix} \delta P_x \\ \delta P_y \\ \delta P_z \end{bmatrix} = \epsilon_0 \begin{bmatrix} 0 & 0 & 0 \\ 0 & 0 & -\delta\epsilon_{23} \\ 0 & -\delta\epsilon_{23} & 0 \end{bmatrix} \begin{bmatrix} 0 \\ E_y^\omega \\ 0 \end{bmatrix} \quad (42)$$

It is noted that perturbation in the permeability tensor induced by electric field E_y^e

gives rise to the perturbation in the optical wave E_y^ω written by $\delta P_z = -\epsilon_0 \delta\epsilon_{23} E_y^\omega$.

3. TE↔TM Mode Converter

If the electric field E_y^e is applied to a LiNbO₃ crystal with the optical wave TM-polarized in the y direction, the TE polarized optical field is obtained by the perturbation polarization δP_z in z direction denoted as

$$[P_{pert}]_z = \epsilon_0 \delta\epsilon_{23} E_y^\omega \quad (43)$$

The TE↔TM mode conversion between two codirectional and orthogonal modes is described by the coupled mode equations

$$\begin{aligned} \frac{dA_m}{dx} &= -i\kappa B_m e^{-i\Delta\beta x} \\ \frac{dB_m}{dx} &= -i\kappa A_m e^{i\Delta\beta x} \end{aligned} \quad (44)$$

where A_m and B_m are complex amplitudes of the two coupled optical waves, $\Delta\beta = \beta_{TM} - \beta_{TE}$ and the coupling coefficient κ is obtained by [7], [11]

$$\kappa = \frac{1}{2} (n_e n_o)^{3/2} k_0 r_{51} E_y^e \quad (45)$$

Assuming the boundary conditions

$$\begin{aligned} A_m(x=0) &= 0 \\ B_m(x=0) &= B_0 \end{aligned} \quad (46)$$

the solutions of equation 44 are obtained as

$$\begin{aligned} A_m(x) &= -B_0 e^{-\delta x} \frac{\kappa}{\sqrt{\kappa^2 + \delta^2}} \sin(\sqrt{\kappa^2 + \delta^2} x) \\ B_m(x) &= B_0 e^{-\delta x} \left[\cos(\sqrt{\kappa^2 + \delta^2} x) - \frac{i\delta}{\sqrt{\kappa^2 + \delta^2}} \sin(\sqrt{\kappa^2 + \delta^2} x) \right] \end{aligned} \quad (47)$$

where $\delta \equiv \frac{1}{2}(\beta_{TM} - \beta_{TE})$. When the two modes are phase matched, we have the simpler solution

$$\begin{aligned} A_m &= -B_0 \sin(\kappa x) \\ B_m &= B_0 \cos(\kappa x) \end{aligned} \quad (48)$$

The plot of the normalized powers $|A_m(x)/B_0|^2$ and $|B_m(x)/B_0|^2$ is illustrated in Fig. 6.

The shortest coupling length L for full power transfer is denoted by

$$L = \frac{\pi}{2\kappa} \quad (49)$$

Full power transfer requires phase-matching condition that $\beta_{TM} = \beta_{TE}$ in the uniform

waveguide structure and $\beta_{TM} - \beta_{TE} = 2\pi/\Lambda$ in the periodic structure (Fig. 7). In Fig.

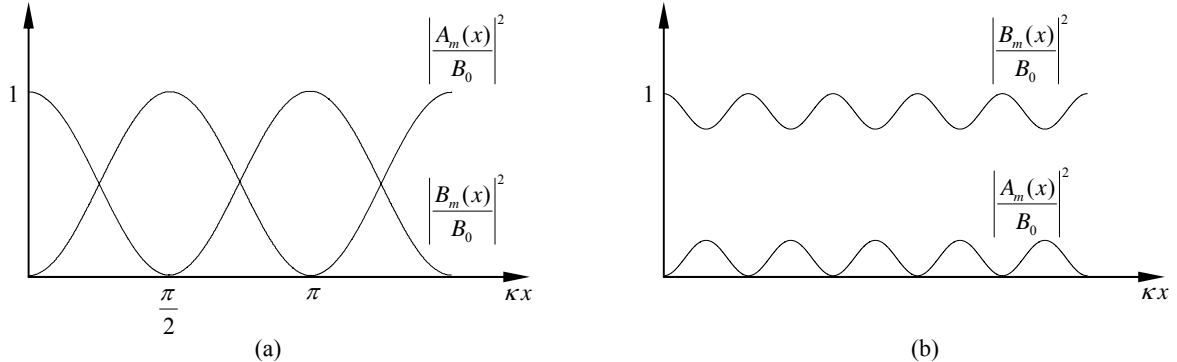


Fig. 6. Power transfer between two coupled optical waves. (a) phase-matched conditon, (b)unmatched conditions

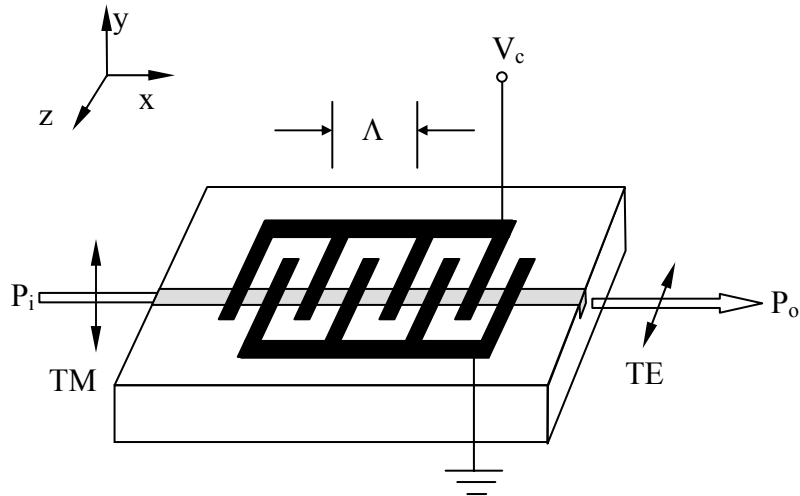


Fig. 7. Periodic electrode structure for electrooptically induced TE-TM coupling

7, the periodicity of the structure compensates for the difference between the two propagation constants. Assuming the phase-matching condition at a certain wavelength λ , the polarization converter behaves as a wavelength filter and the optical bandwidth of $\text{TE} \leftrightarrow \text{TM}$ conversion becomes [12]

$$\Delta\lambda_{FWHM} \approx 0.8 \left(\frac{\Lambda}{L} \right) \lambda \quad (50)$$

where $\Delta\lambda_{FWHM}$ is the 3-dB bandwidth (FWHM).

CHAPTER III

DESIGN OF ELECTROOPTIC MATCHED FILTER

A. The Principal Characteristics of EMF

The electrooptic matched filter (EMF) utilizes polarization coupling produced by the Pockels effect in a periodic waveguide structure. A cross-sectional view of interdigital electrodes implemented on LiNbO₃ is shown schematically in Fig. 8. The voltage V is applied to the electrodes and establishes periodic electric fields in the single-mode waveguide. The x component of electric field provides TE↔TM mode conversion induced by $\delta\epsilon_{23}$ perturbation in the permeability tensor via the electrooptic coefficient r_{51} . The mode conversion is a wavelength selective process. The most efficient wavelength λ_0 is found by the phase-matching condition as

$$\lambda_0 = \Lambda |n_{TM} - n_{TE}| \quad (51)$$

where Λ is the period of interdigital electrodes and n_{TM} and n_{TE} are the effective refractive indices of the TM and TE modes. It is noted that the EMF is polarization independent since TE→TM and TM→TE conversion are reciprocal processes.

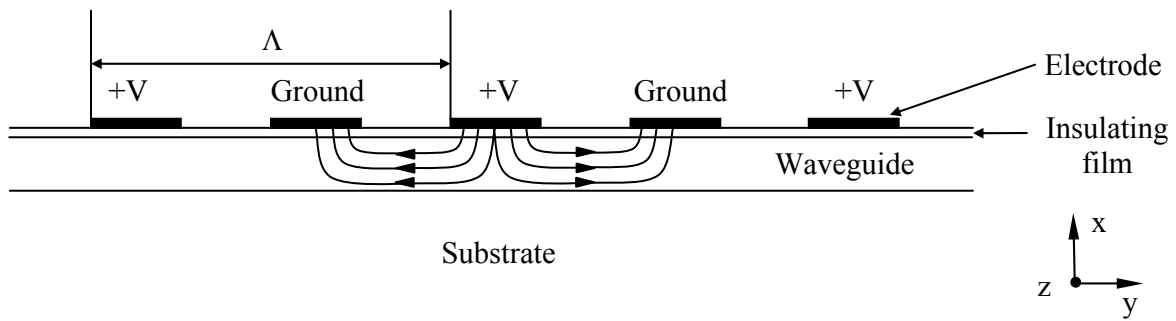


Fig. 8. Cross-sectional view of electrodes

Wavelength selection is achieved if the first order phase-matching condition $\Delta = 0$ is satisfied, where the phase mismatch constant Δ is [13]

$$\Delta = \frac{2\pi\nu(n_{TM} - n_{TE})}{c} \pm \frac{2\pi}{\Lambda} \quad (52)$$

and c and ν are the light velocity in free space and the optical frequency, respectively. Assuming the selected optical frequency ν_j , Δ is large and the efficiency of polarization conversion is reduced as the frequency is slightly different from ν_j . Hence, the tuning mechanism can be described by applying the voltage to the electrodes to nullify Δ at any desired frequency. The change in birefringence induced by the electric field makes up for the frequency deviation from ν_j of equation 52. Assuming that the birefringence $n_{TM} - n_{TE}$ is equal to $n_1 - n_3$ the difference between principal refractive indices of LiNbO₃, the deviation in frequency ν from ν_j is derived from equation 52 as below

$$\nu - \nu_j = \frac{c\Delta}{2\pi(n_{1g} - n_{3g})} \quad (53)$$

where n_{1g} and n_{3g} are the group refractive indices of the birefringent substrate material.

Sidelobe suppression can be accomplished by implementing a suitable coupling strength distribution along the length of a waveguide. Coupling interaction controlled by applying a weighting function to the electrodes has been reported [14], [15]. In the EMF design, a raised cosine apodization is used to achieve highly suppressed sidelobes. The sidelobe levels are suppressed to below -10 dB by applying a raised cosine apodizing function

$$\kappa(y) = \kappa_0 + 0.5\kappa_0 \cos\left[2\pi\left(\frac{y}{L} - 0.5\right)\right] \quad (54)$$

where the uniform coupling coefficient κ_0 is denoted by $\kappa_0 = \pi / 2L$ from equation 49.

The TE \leftrightarrow TM polarization conversion of EMF is described by the coupled mode equations

$$\begin{aligned} \frac{dA(y)}{dy} &= -i\kappa B(y)e^{-i\Delta y} \\ \frac{dB(y)}{dy} &= -i\kappa A(y)e^{i\Delta y} \end{aligned} \quad (55)$$

for the case of codirectional coupling and will be analyzed in detail at section 3.4. Here, $A(y)$ and $B(y)$ are the complex amplitude of the two coupled modes.

B. The EMF Structure for Two Sidebands

In previous tunable electrooptic filters, the same voltage was supplied to each set of interdigital electrodes for mode conversion while another separate voltage applied outside TE \leftrightarrow TM mode conversion region was utilized to perform tuning of the wavelength [12], [15]. In contrast, the EMF operates by applying programmable voltages to independent electrode sets as shown in Fig. 9. The array of electrode sets is formed on the waveguide which is fabricated on an x-cut y-propagating LiNbO₃ substrate by Ti diffusion. The EMF is composed of 8 sets of interdigital electrodes to tune 5 wavelength channels according to the relation $N = P / 2 + 1$, where N is the number of selectable channels and P is the number of electrode sets. The spatial period of the interdigital electrodes Λ is $21 \mu m$. The period of electrode sets Π is $200 \cdot \Lambda$ and the length of single mode conversion region l_c is $(179 + 3/4) \cdot \Lambda$. The ideal

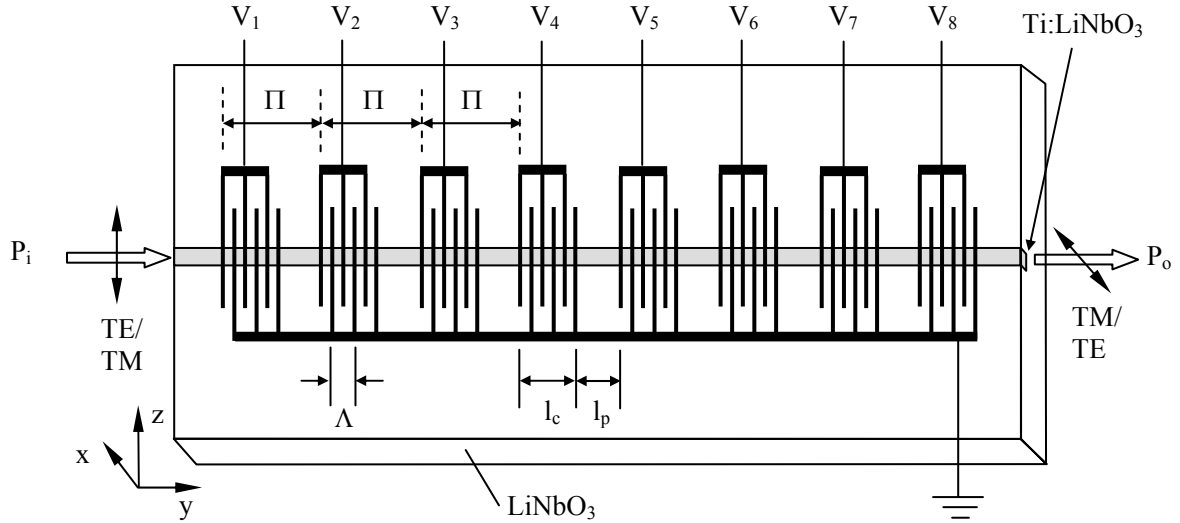


Fig. 9. Schematic diagram of the EMF structure and orientation for two sidebands

coupling strength distribution along the length of the electrode sets in the structure for two sidebands is

$$\kappa_j(y) = S(y) \cos(\Delta_j y), \quad j = 1, 2, 3, \dots, N \quad (56)$$

where $S(y)$ is the apodization function and

$$\Delta_j = \frac{2\pi |n_{1g} - n_{3g}| (\nu_j - \nu_0)}{c} \quad (57)$$

It is noted that in the phase-matched condition, the integral of the coupling coefficient over the interaction length L is given by

$$\int_0^L \kappa dy = \frac{\pi}{2} \quad (58)$$

for a complete $\text{TE} \leftrightarrow \text{TM}$ power conversion.

The j 'th frequency channel is selected by applying a periodic set of voltages V_{jp} , $p = 1, 2, 3, \dots, P$, to the electrode sets. In equation 55, the coupling coefficient is real,

so that frequency channels equally separated from the center frequency ν_0 are selected in the structure for two sidebands, where

$$\nu_0 = \frac{c}{|n_{TM} - n_{TE}| \Lambda} \quad (59)$$

The algorithm to select frequency channels is shown in Fig. 10. At the center frequency ν_0 , $\Delta_0 = 0$ and the coupling coefficient κ is given by [12]

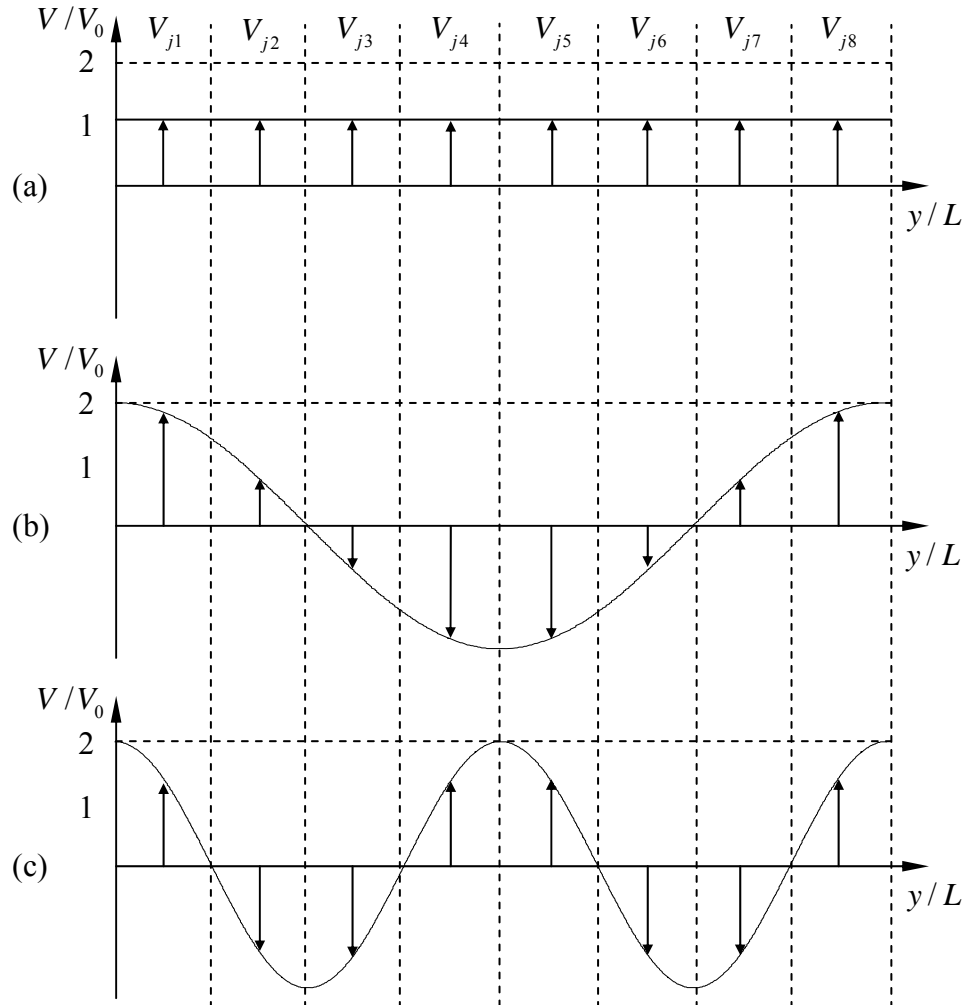


Fig. 10. Selection of voltages in the structure of two sidebands. (a) for $j = 0$ sideband,
(b) for $j = \pm 1$ sidebands, (c) for $j = \pm 2$ sidebands

$$\kappa = \frac{\pi \Gamma n^3 r_{s1} E_x}{\lambda_0} \quad (60)$$

where Γ is an overlap parameter of the applied electric field with the optical waveguide mode and $n = \sqrt{n_1 n_3}$. Suppose that the width and the spacing for the interdigital electrodes are equal to $\Lambda/4$, the uniform coupling voltage for selecting V_0 is written from equations 57 and 59 by

$$V_0 = \frac{\lambda_0 \Lambda}{2 \Gamma n^3 r_{s1} L} \quad (61)$$

In this research, V_0 is obtained experimentally to optimize the polarization conversion. The ratio of V_{jp} to the V_0 are given in Table 1 where the voltages for the raised cosine apodization are obtained by using equation 54.

C. The EMF Structure for Single Sideband

The modified EMF structure to select only a single sideband is shown in Fig.11. The length of an interdigital electrode set is periodically altered between

Table 1. The ratio of V_{jp} applied to p'th channel to V_0 for the selection of j'th frequency channel in the structure of two sidebands

j, channel		p, the number of electrode set							
		1	2	3	4	5	6	7	8
Without apodization	0	1	1	1	1	1	1	1	1
	± 1	1.848	0.765	-0.765	-1.848	-1.848	-0.765	0.765	1.848
	± 2	1.414	-1.414	-1.414	1.414	1.414	-1.414	-1.414	1.414
With raised cosine apodization	0	0.538	0.809	1.191	1.462	1.462	1.191	0.809	0.538
	± 1	0.994	0.619	-0.912	-2.701	-2.701	-0.912	0.619	0.994
	± 2	0.761	-1.144	-1.685	2.067	2.067	-1.685	-1.144	0.761

$\Pi_\alpha = (200 - 1/4)\Lambda$ and $\Pi_\beta = (200 + 1/4)\Lambda$. The regions of Π_α and Π_β cause in-phase and quadrature coupling, respectively. The coupling coefficient is complex and is written by

$$\kappa_j(y) = S(y)e^{i\Delta_j y} \quad (62)$$

For the in-phase and quadrature coupling, the coupling coefficient κ_j is written by

$$\begin{aligned} \kappa_j(y) &= S(y)\cos(\Delta_j y), \quad j = \pm(2n-1) \\ \kappa_j(y) &= iS(y)\sin(\Delta_j y), \quad j = \pm 2n \end{aligned} \quad (63)$$

respectively, with $n = 1, 2, 3, \dots$. In the similar manner to the structure for two sidebands, the treatment to select the p'th electrode voltage for j'th frequency channel for single sideband is illustrated in Fig. 12. The voltages for $j = -1$ and $j = -2$ can be obtained from Fig. 12 (b) and (c) with the opposite sign for the even voltages. The selected voltages for j'th frequency channel satisfy the relation

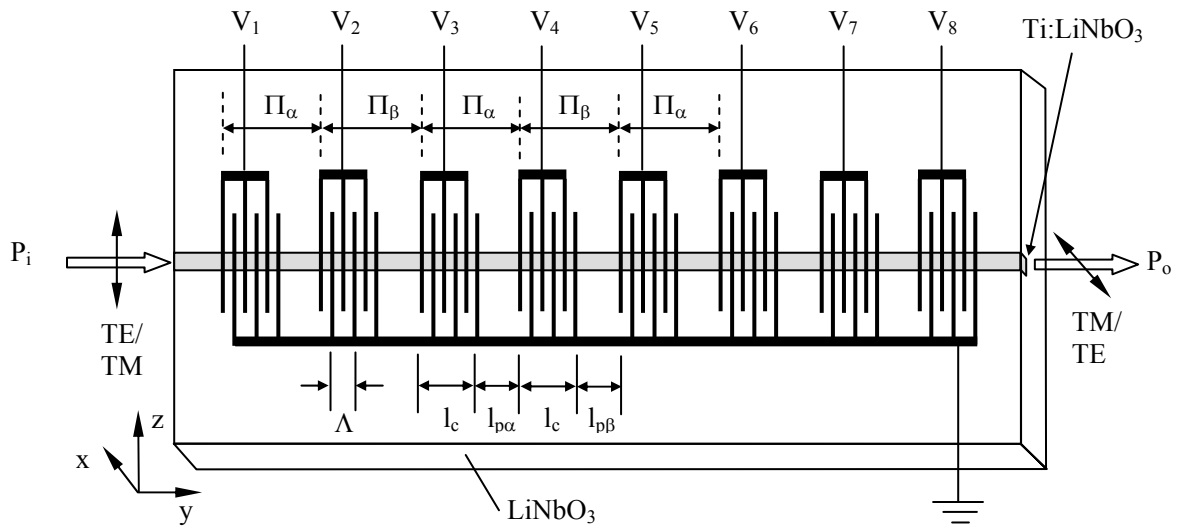


Fig. 11. Modified configuration in the series of electrodes for a single sideband

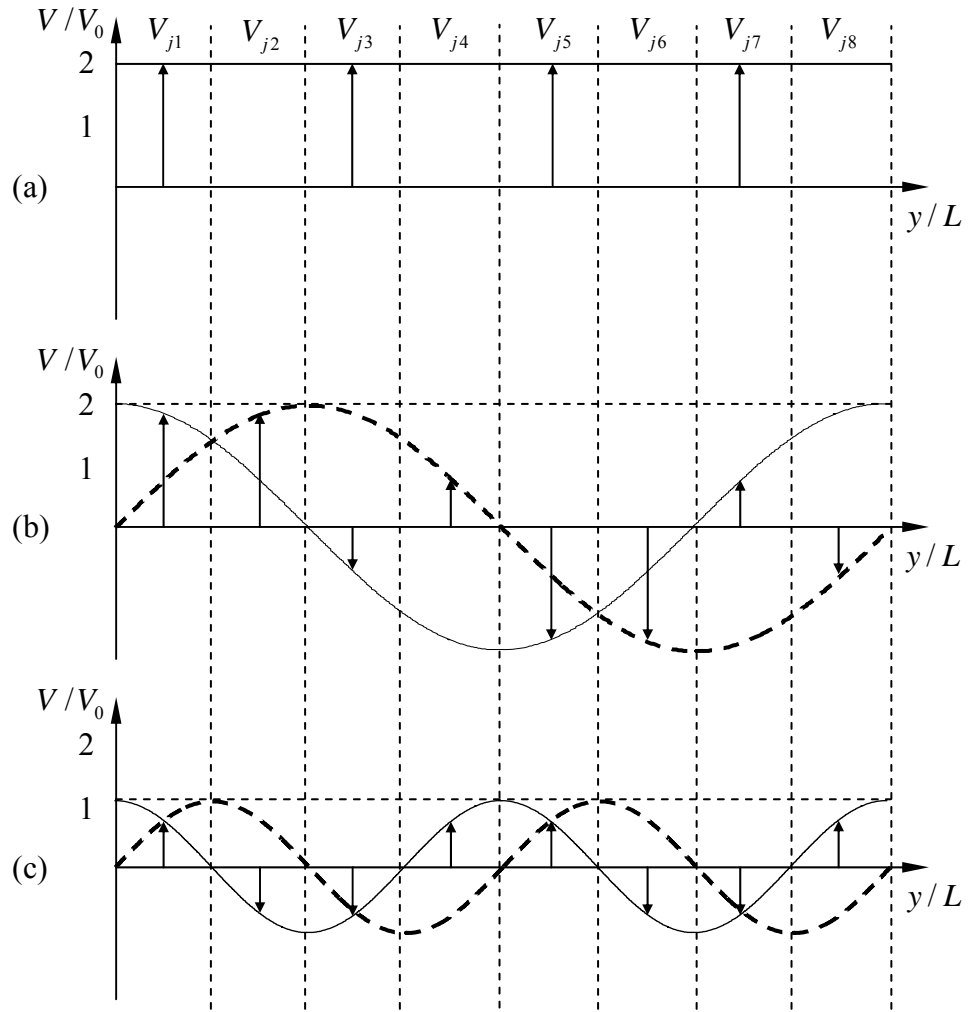


Fig. 12. Selection of voltages in the structure of a single sideband. (a) for $j = 0$ sideband, (b) for $j = 1$ sideband, (c) for $j = 2$ sideband

$$\int_0^L \kappa_j(y) e^{-i\Delta_k y} dy = \frac{\pi}{2} \delta_{jk} \quad (64)$$

with $\delta_{jk} = 1$ if $j = k$ and $\delta_{jk} = 0$ otherwise. Table 2 summarizes the ratio of the voltages applied to electrode sets V_{jp} to the uniform coupling voltage V_0 for both an unapodized and a raised cosine apodized filter transmission. It is found that the EMF acceptably has an expected filter characteristics, although the voltages applied to the electrode sets vary in a discrete manner to select both two sidebands and single

Table 2. The ratio of V_{jp} applied to p'th channel to V_0 for the selection of j'th frequency channel in the structure of single sideband

j, channel		p, the number of electrode set							
		1	2	3	4	5	6	7	8
Without apodization	-2	0.707	-0.707	-0.707	0.707	0.707	-0.707	-0.707	0.707
	-1	1.848	-1.848	-0.765	-0.765	-1.848	1.848	0.765	0.765
	0	2	0	2	0	2	0	2	0
	1	1.848	1.848	-0.765	0.765	-1.848	-1.848	0.765	-0.765
	2	0.707	0.707	-0.707	-0.707	0.707	0.707	-0.707	-0.707
With raised cosine apodization	-2	0.380	-0.572	-0.842	1.034	1.034	-0.842	-0.572	0.380
	-1	0.994	-1.494	-0.912	-1.119	-2.701	2.201	0.619	0.412
	0	1.076	0	2.383	0	2.924	0	1.617	0
	1	0.994	1.494	-0.912	1.119	-2.701	-2.201	0.619	-0.412
	2	0.380	0.572	-0.842	-1.034	1.034	0.842	-0.572	-0.380

sideband.

D. Matrix Formulation and Simulation Results

The EMF of Fig. 9 and Fig. 11 consists of 8 identical TE↔TM mode coupling regions spaced by 10% of the width of a set. The effect of each individual element, either a coupling region or a propagation region, can be analyzed in a systematic manner by using a matrix formulation [13], [16]. In a matrix method, each optical element is described by a 2×2 matrix. The overall transfer matrix of the whole system is given by the product of all the individual element matrices. In the structure for two sidebands, the effect of polarization conversion in the j'th coupling region and of phase shift in the spacing between electrodes is written by

$$\mathbf{E}_{j+1} = \mathbf{M}_j \mathbf{E}_j \quad (65)$$

The vector \mathbf{E}_j is given by

$$\mathbf{E}_j = \begin{pmatrix} E_j^{TE} \\ E_j^{TM} \end{pmatrix}, \quad j = 1, 2, 3, \dots, P \quad (66)$$

where E_j^{TM} and E_j^{TE} are the electric field amplitudes of two polarization modes just prior to the j 'th coupling region and the 2×2 transfer matrix \mathbf{M}_j is given by $\mathbf{M}_j^C \mathbf{M}^\Phi$. Here, the matrix \mathbf{M}^Φ describes the phase shift occurring at the propagation region between adjacent coupling regions, which is given by

$$\mathbf{M}^\Phi = \begin{bmatrix} e^{-i\frac{\phi}{2}} & 0 \\ 0 & e^{i\frac{\phi}{2}} \end{bmatrix} \quad (67)$$

where the experienced phase retardation is

$$\phi = (\beta_1 - \beta_2)l_p \quad (68)$$

with $\beta_1 = 2\pi\nu n_{TE}/c$, $\beta_2 = 2\pi\nu n_{TM}/c$ and $l_p = \Pi - l_c$. The matrix \mathbf{M}_j^C representing the effect of polarization conversion at the j 'th coupling region is in general written by adapting the well known solution of equation 55 [11], [17]

$$\mathbf{M}_j^C = \begin{bmatrix} a_c e^{-i(\beta_1 + \frac{\Delta}{2})l_c} & b_c e^{-i(\beta_1 + \frac{\Delta}{2})l_c} \\ -b_c^* e^{-i(\beta_2 - \frac{\Delta}{2})l_c} & a_c e^{-i(\beta_2 - \frac{\Delta}{2})l_c} \end{bmatrix} \quad (69)$$

where

$$\begin{aligned} a_c &= \cos(\sqrt{\kappa^2 + \delta^2}l_c) + i \frac{\delta}{\sqrt{\kappa^2 + \delta^2}} \\ b_c &= -i \frac{\delta}{\sqrt{\kappa^2 + \delta^2}} \sin(\sqrt{\kappa^2 + \delta^2}l_c) \end{aligned} \quad (70)$$

and z^* is used to denote the complex conjugate of z . The EMF consists of the first coupling region and the $P - 1$ pairs of alternating polarization conversion region and the spacing between them, so that the conversion matrix is given by

$$C = \left(\prod_{j=2}^P \mathbf{M}_j^C \mathbf{M}^\Phi \right) \mathbf{M}_1^C \quad (71)$$

Assuming that the TE polarization mode is excited at the input of EMF and its amplitude is normalized to 1, the power coupling efficiency is written by

$$PCE = |C_{12}|^2 \quad (72)$$

where C_{12} is the off-diagonal element of the matrix C .

The performance characteristics for channel 0, ± 1 , and ± 2 in the structure for two sidebands are shown in Fig. 13 (a), (b), and (c) where the sidelobe suppression by raised cosine apodization is shown in the solid curve compared with the unapodized dashed line. As can be observed, the sidelobe level is reduced at the expense of its bandwidth performance by applying a raised cosine apodization function along the length of the EMF coupling region.

Likewise, the transfer matrix for single sideband configuration shown in Fig. 11 can be described except that the matrix \mathbf{M}^Φ in equation 71 is replaced with $\mathbf{M}^{\Phi a}$ if j is the even number and $\mathbf{M}^{\Phi b}$ otherwise. Here, the matrices $\mathbf{M}^{\Phi a}$ and $\mathbf{M}^{\Phi b}$ are given in the similar form to equation 67, while ϕ_α and ϕ_β are used instead of ϕ , respectively where

$$\begin{aligned} \phi_\alpha &= (\beta_1 - \beta_2)l_{p\alpha} \\ \phi_\beta &= (\beta_1 - \beta_2)l_{p\beta} \end{aligned} \quad (73)$$

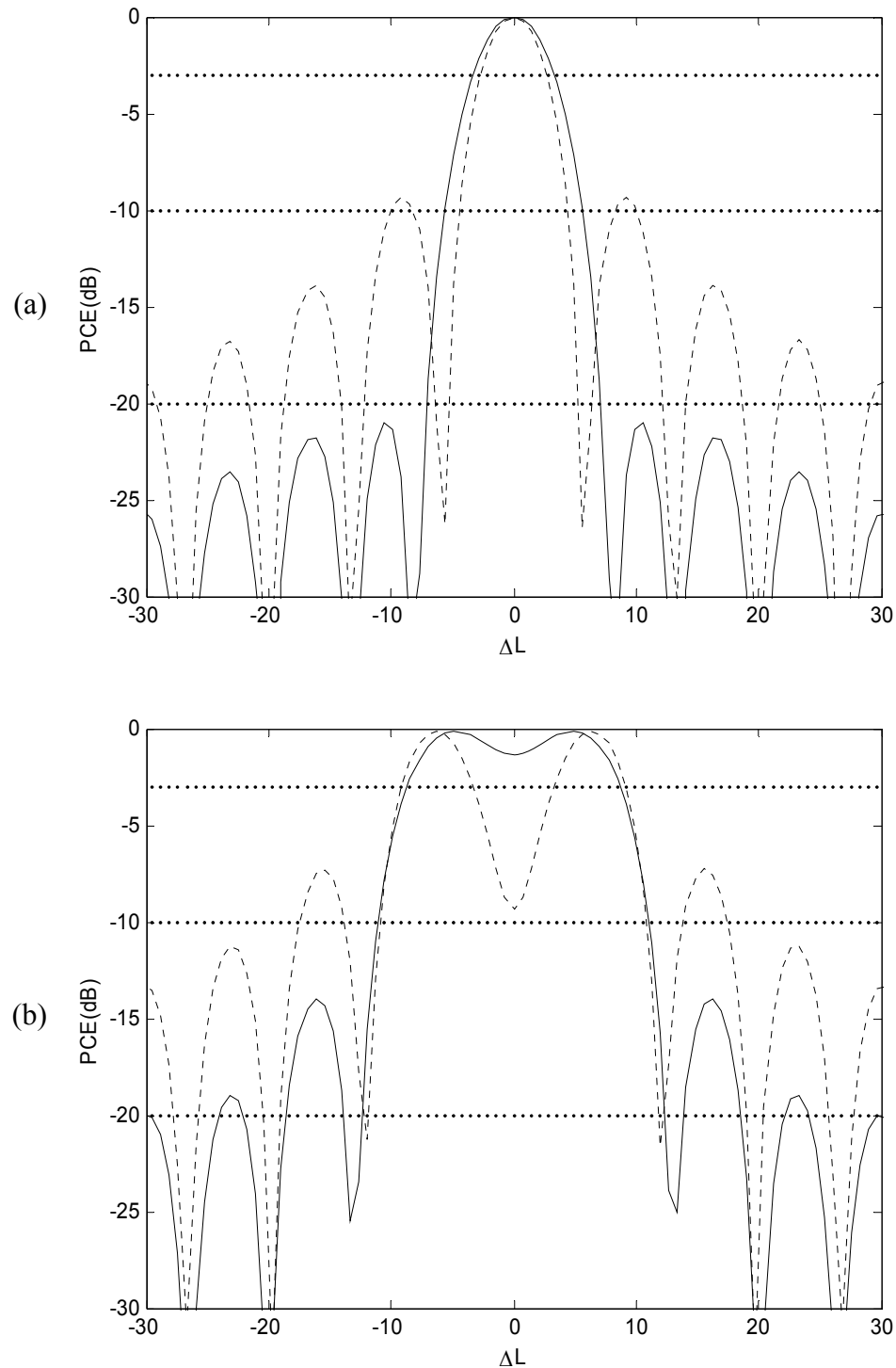


Fig. 13. Simulated performances in the structure of two sidebands. (a) for channel 0, (b) for channel ± 1 , (c) for channel ± 2

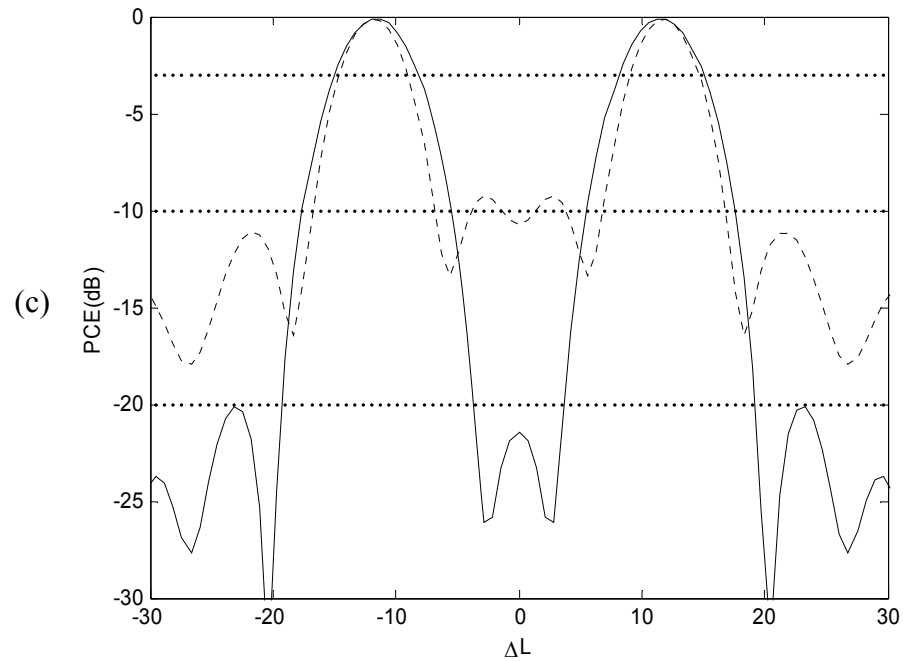


Fig. 13. Continued

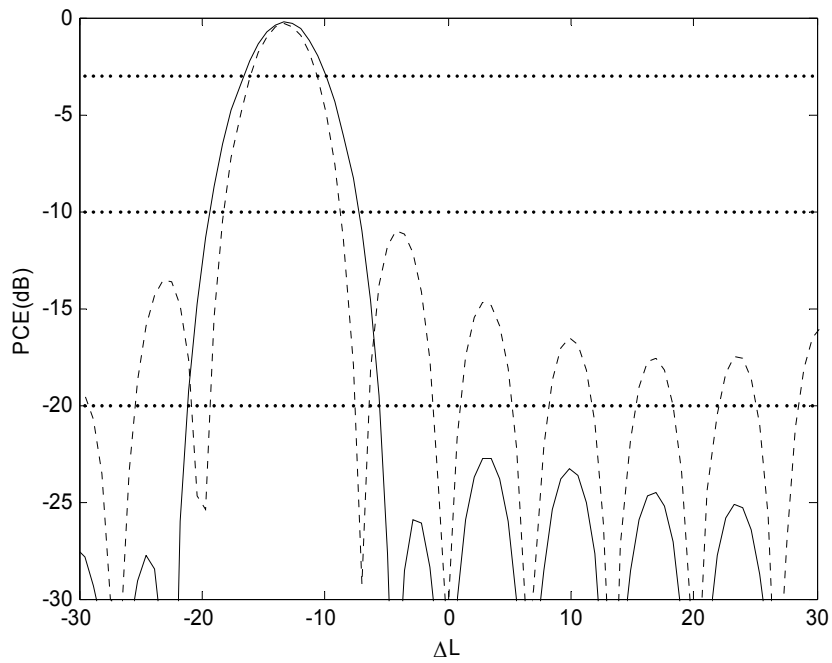


Fig. 14. Simulated performance in the single sideband configuration for channel -2

with $l_{p\alpha} = \Pi_\alpha - l_c$ and $l_{p\beta} = \Pi_\beta - l_c$. The calculated power conversion spectra for channel -2 in the structure of single sideband are shown in Fig. 14. The sidelobe suppression reduced by a raised cosine apodization is shown by the solid curve. It is observed that a raised cosine weighting results in sidelobe levels below -20 dB.

CHAPTER IV

ELECTRONIC DRIVING CIRCUIT FOR EMF

A. Digital-to-Analog Converter Driving Circuit

The EMF is controlled by applying different voltages to each electrode set independently. A digital-to-analog converter (DAC) independently controls the voltage on each electrode. The AD5379 from Analog Devices contains 40 DACs in one package and provides the maximum output voltages span of 17.5 V, corresponding to an output range of -8.75 V to $+8.75$ V. In this research, programmable data inputs are loaded from a personal computer (PC) memory into the AD5379 input registers by a serial interface and are decoded into the DAC output at a selected channel (Fig. 15).

Fig 16 shows the electronic driving circuit configuration for the EMF. The PC is

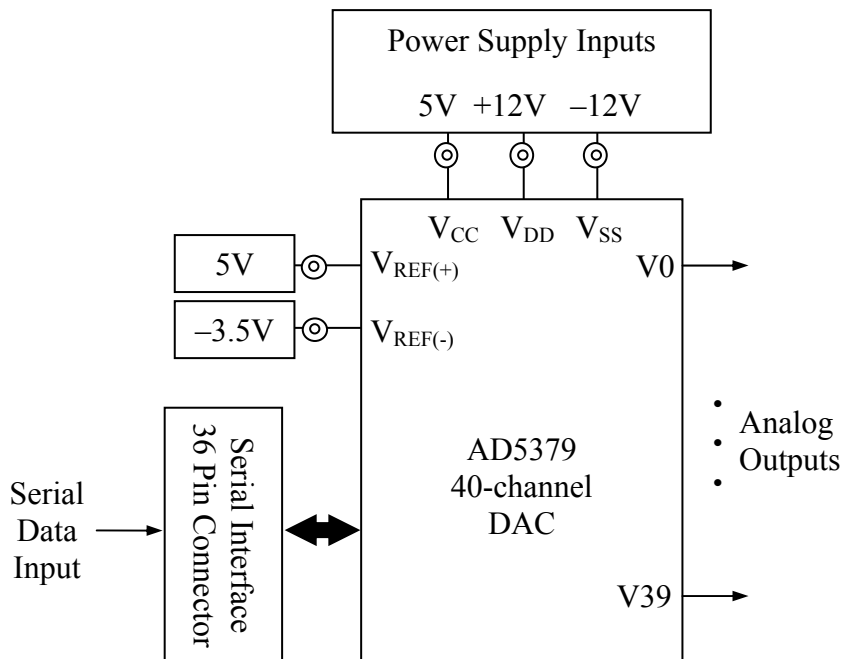


Fig. 15. AD5379 board

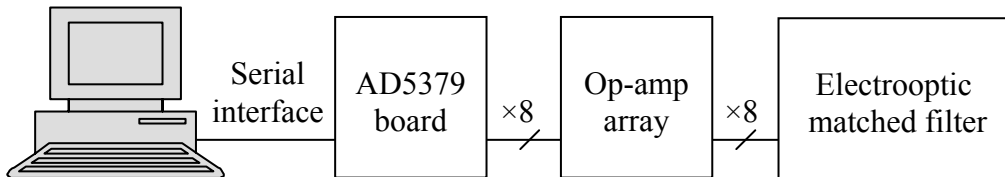


Fig. 16. Electronic driving circuit setup

connected to the AC5379 board by a Centronics cable. The DAC output voltages are insufficient to directly drive the EMF, so an external op-amp array is utilized to obtain higher voltages.

B. Loading DAC Channels

Analog Devices provides the PC software for control of DACs. Fig. 17 shows the graphic user interface to load each channel in the DAC menu of the software. All channels or each channel can be loaded manually with the entered DAC code. The AD5379 accepts 14-bit data word format in Table 3 from the serial interface. The hexadecimal code entered at the field “Enter Data (Hex)” in Fig. 17 can be decoded as

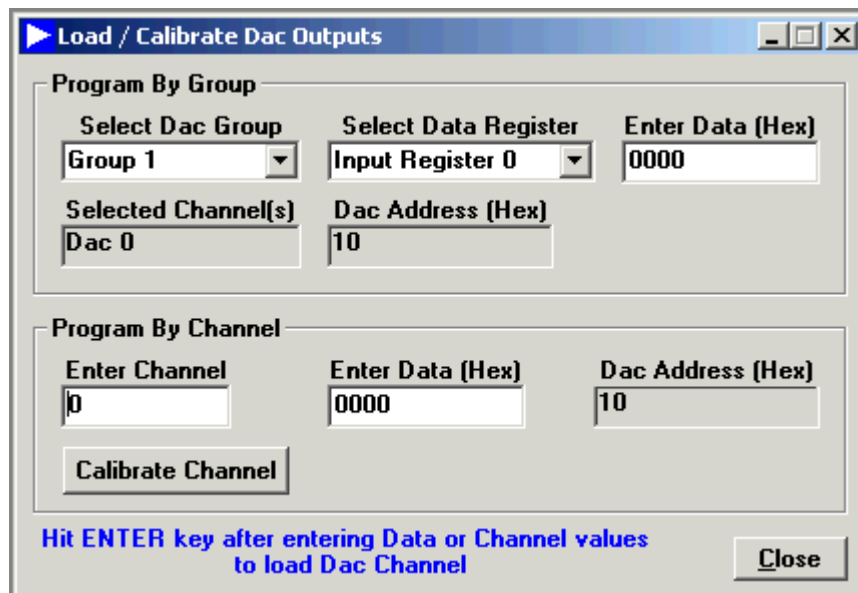


Fig. 17. Load DAC channels

Table 3. 14-bit data word format

14-bit data word	Hexadecimal	Offset
11 1111 1111	3FFF	+8191
11 1111 1111	3FFE	+8190
10 0000 0000	2001	+1
10 0000 0000	2000	0
01 1111 1111	1FFF	-1
00 0000 0000	0001	-8191
00 0000 0000	0000	-8192

follows:

$$V = \left(V_{OUT_{\max}} \times \frac{HEX2DEC(Hex) - 8192}{8192} \right) \times G \quad (74)$$

where $V_{OUT_{\max}} \simeq V_{OUT_{\max(+)}} \simeq -V_{OUT_{\max(-)}}$ is a maximum DAC output voltage and G is the voltage gain of op-amp. Here, $HEX2DEC(Hex)$ is a function that converts a hexadecimal number Hex to decimal.

CHAPTER V

EXPERIMENTAL RESULTS

A. Experimental Configuration

Optical testing was carried out using the amplified spontaneous emission (ASE) from a broadband light source of an erbium-doped fiber pumped by a 980 nm laser diode. The ASE spectrum of an erbium-doped fiber amplifier is 40 nm wide with a peak power at a wavelength of 1530 nm. Fig. 18 shows the schematic diagram of experimental setup. The input polarization is selected to be TE or TM by rotating the end of the polarizing fiber. External electronic circuits drive 8 independent sets of electrodes by using a DAC array from Analog Devices, as described in Chapter IV. The transmitted beam, after it passes through the EMF and the optical polarizer, is monitored with an optical spectrum analyzer.

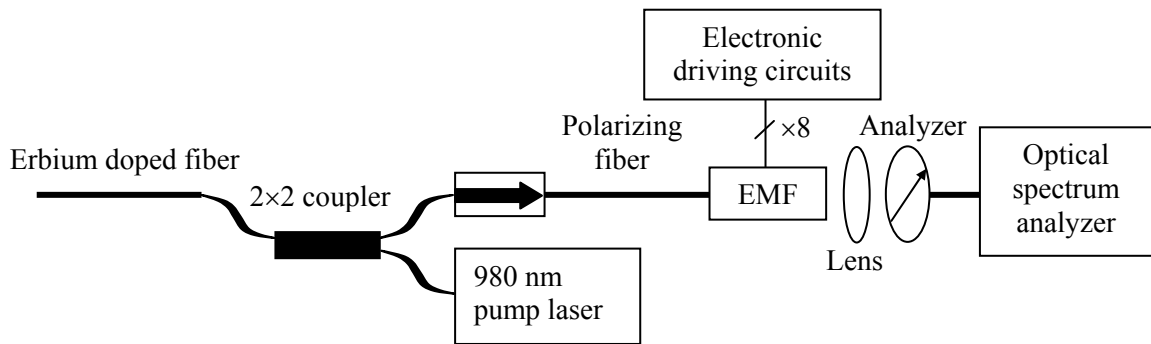


Fig. 18. A schematic diagram of experimental setup

B. Test Results

In the structure for two sidebands, the transfer response of TE \rightarrow TM conversion is shown in Fig. 19. Fig. 19 (a) shows the unapodized output response for the TM mode

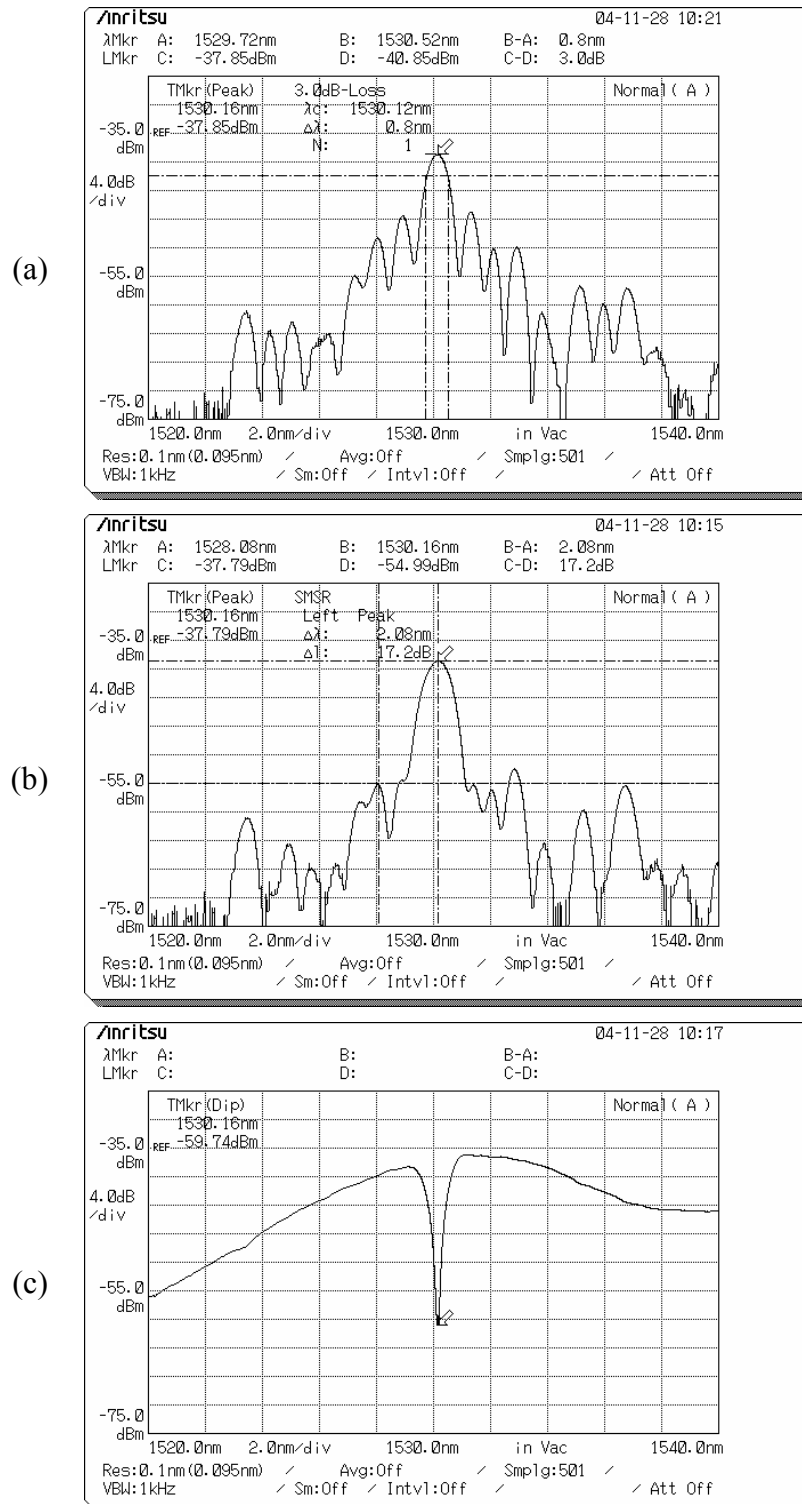


Fig. 19. The optical output power spectra of EMF for TE \rightarrow TM polarization conversion in the structure for two sidebands. (a) unapodized and (b) apodized filter responses of TM mode at channel 0, (c) apodized filter response of TE mode at channel 0, (d) apodized output power responses of TM mode at channel ± 1 and (e) channel ± 2

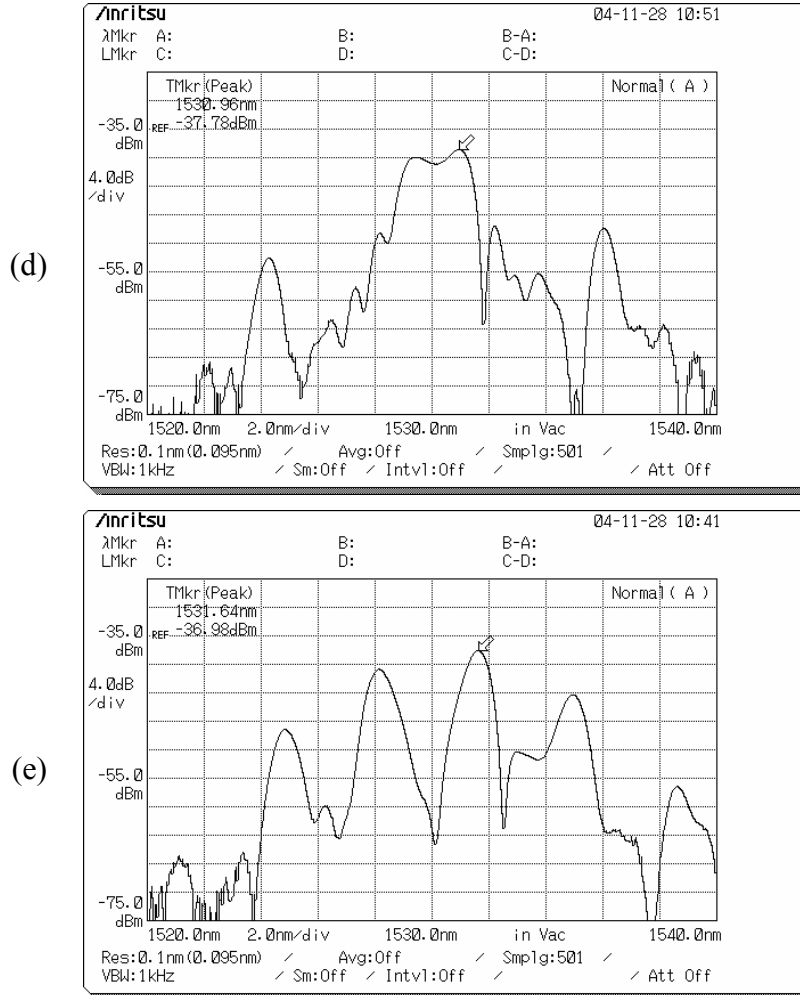


Fig. 19. Continued

at the channel 0 with a uniform coupling voltage $V_0 = 13$ V. As can be observed, the optical bandwidth (FWHM) of 0.8 nm is in close agreement with the calculated value from equation 50. In Fig.19 (b), a sidelobe suppression level better than -17 dB is achieved by applying a raised cosine weighting function to the electrodes along the length of the device at the expense of bandwidth performance. Fig. 19 (c) shows the filter response of the TE polarized mode with the coupling strength apodized. In Fig. 19 (d) and (e), apodized TM mode output responses for channel ± 1 and ± 2 are shown

with wavelength shifted. The filter performance of TM \rightarrow TE polarization conversion is similar to that of TE \rightarrow TM conversion shown in Fig. 19.

Figs. 20, 21 and 22 show theoretical and experimental curves for apodized EMF filter characteristic at channel 0, ± 1 , and ± 2 , respectively. In these figures, only the baseline transmittance of the computer simulation plots was adjusted to approximately match the experimental curves. The results are in good agreement with theory.

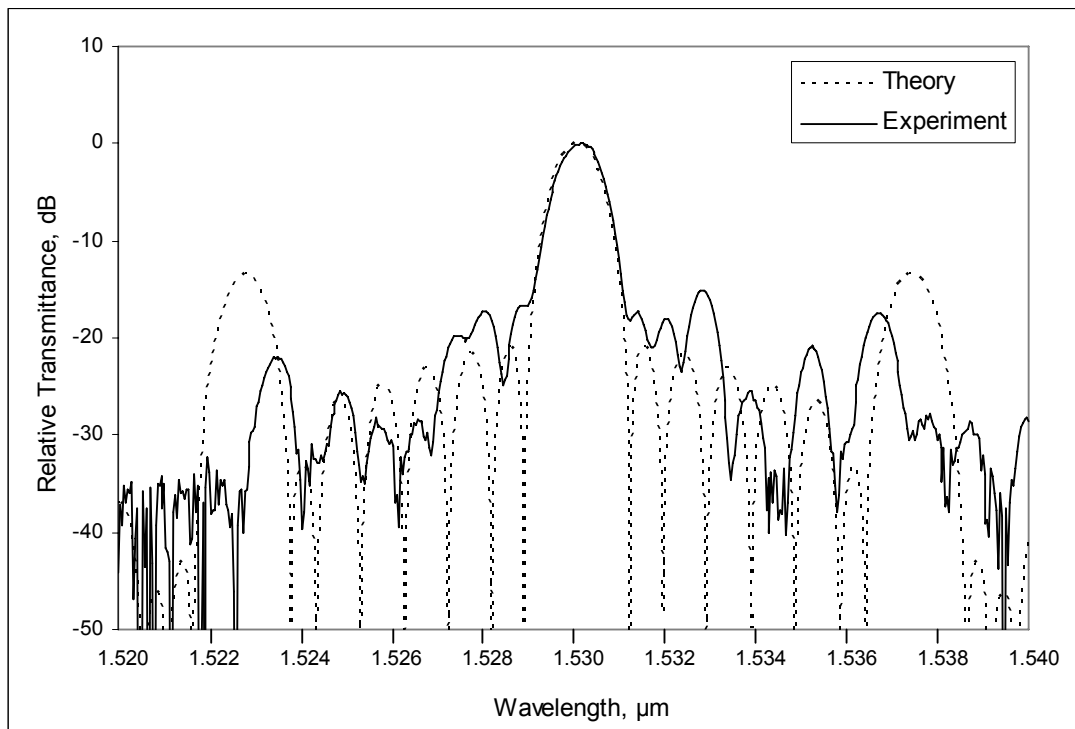


Fig. 20. EMF filter characteristic at channel 0

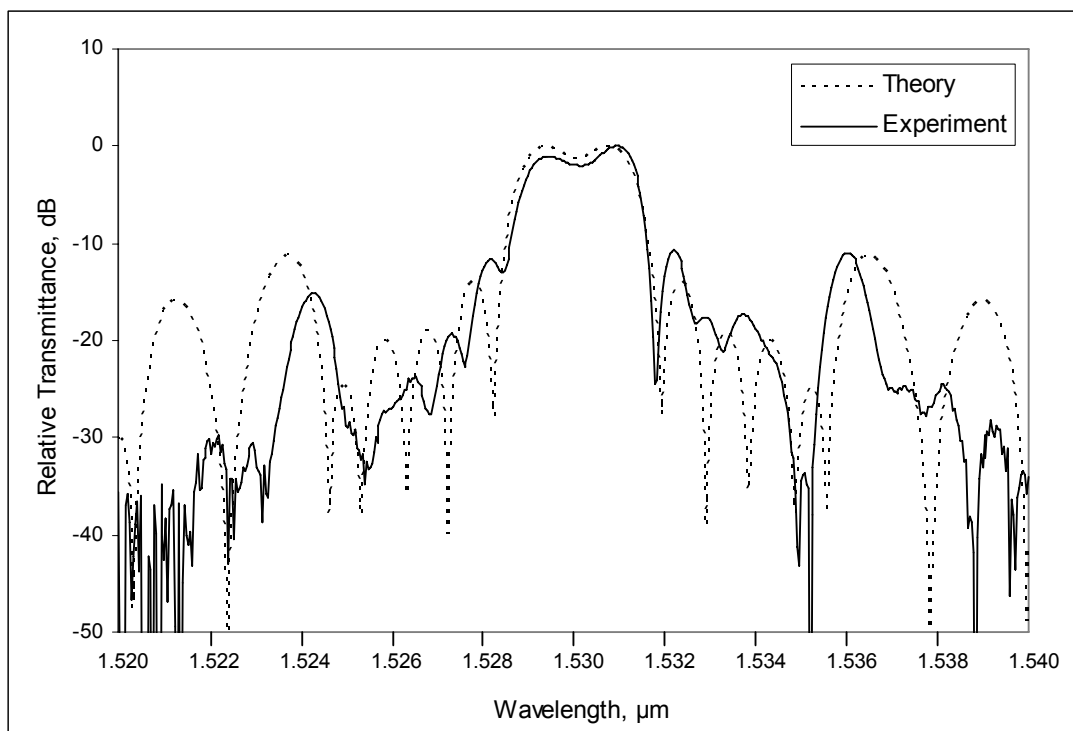


Fig. 21. EMF filter characteristic at channel ± 1

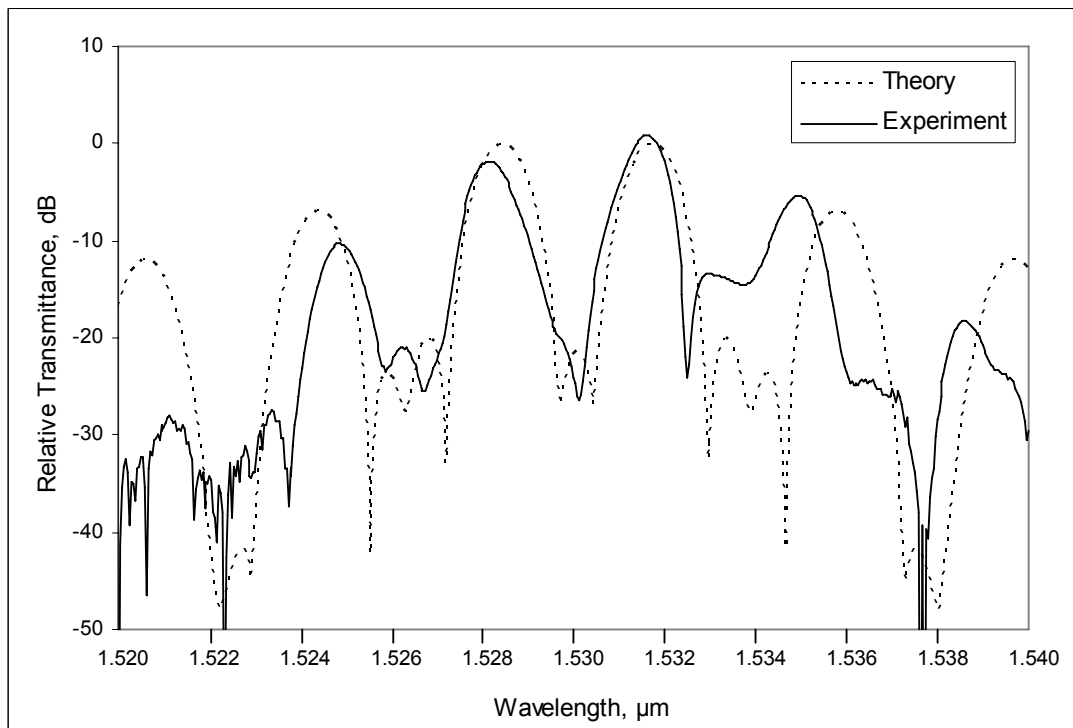


Fig. 22. EMF filter characteristic at channel ± 2

CHAPTER VI

CONCLUSIONS

This thesis presents a theoretical and experimental study of an electrooptic matched filter (EMF) designed for operation in the 1530 nm spectral regime. The device utilizes TE↔TM polarization conversion in a single mode waveguide fabricated in LiNbO₃ by Ti diffusion. The number of selectable frequency channels N is $N = 5$ according to the relation $N = P/2 + 1$ with the number of electrode sets $P = 8$. Channel selection is achieved by applying 8 independent programmable voltages to the electrode sets.

In the structure for two sidebands, the two channels equally separated from the center frequency ν_0 are selected. The modified configuration for single sideband provides the selection of only one channel. The performance of the EMF is inherently independent of the input polarization because of the reciprocal characteristic between TE and TM mode polarization conversion. A spectral tuning range of 3.2 nm for 5 channels is demonstrated in this research without altering bandwidth performance. More channels can be accommodated by increasing the number of electrode sets (e.g., if $P = 198$, then $N = 100$) with the length of the device unchanged.

A tuning speed of less than 50 ns was achieved previously in a LiNbO₃ tunable filter [18], and similar fast tuning is expected in the EMF when suitable electronic driving circuits are supported. The full width at half-maximum (FWHM) of the device is 0.8 nm with no apodization of electrode voltages. The FWHM increases to 1.0 nm

when a raised cosine weighting function is applied to the electrode voltages. Apodization improves the sidelobe suppression from -8.6 dB to -17.2 dB.

CHAPTER VII

RECOMMENDATIONS

In this thesis, the configuration for two sidebands has been tested and demonstrated. Tests of the structure for single sideband were also conducted and showed the transmittance spectra expected from computer simulation. However, the device with 8 electrode sets for single sideband produces unacceptable results, tuning over only +1, 0, and -1 frequency channels. The structure for single sideband with more than 8 electrode sets can realize good filter characteristics showing close agreement with prediction.

In the current setup, voltages higher than 10 V are applied to drive the EMF from external circuitry. These voltages are out of the range which can be applied by the DAC used in this research and are amplified by op-amps to overcome the voltage limit of the DAC. New electronic components to provide higher voltage supply can facilitate the experiments. Additionally, the effect of oxide layer on an overlap parameter Γ should be analyzed to predict exact voltages applied to electrodes.

Based on the results presented in Chapter IV, the EMF can be configured for a 4 port add-drop multiplexer and a two port bandpass filter with a Mach-Zehnder interferometer structure. Here, the two arms in the Mach-Zehnder utilize EMF polarization converters.

The spectral tuning range of the EMF for coarse WDM application can be improved by using a LiTaO₃ substrate because the birefringence of LiTaO₃ is much

less than that of LiNbO₃, leading to approximately 20 times the tuning range for a given device length compared with LiNbO₃.

REFERENCES

- [1] R. Ramaswani and K. N. Silvarajan, *Optical Networks: A Practical Perspective*, 2nd Edition. San Francisco, CA: Morgan Kaufmann Publishers, 2001.
- [2] R. Ramaswani, “Optical fiber communication: From transmission to networking,” *IEEE Commun. Mag.*, pp. 138–147, May 2002.
- [3] B. Hirosaki, K. Emura, S. Hayano, and H. Tsutsumi, “Next-generation optical networks as a value creation platform,” *IEEE Commun. Mag.*, pp. 65–71, Sep. 2003.
- [4] D. Sadot and E. Boimovich, “Tunable optical filters for dense WDM networks,” *IEEE Commun. Mag.*, pp. 50-55, Dec. 1998.
- [5] W. Warzanski, F. Heismann, and R. C. Alferness, “Polarization-independent electro-optically tunable narrow-band wavelength filter,” *Appl. Phys. Lett.*, vol. 53, pp. 13–15, July 1988.
- [6] Z. Tang, O. Eknayan and H. F. Taylor, “Polarisation-independent electro-optically tunable wavelength filter in LiTaO₃,” *Electron. Lett.*, vol. 30, pp. 1758–1759, 1994.
- [7] A. Yariv, *Optical Electronics in Modern Communications*, 5th Edition. New York: Oxford University Press, 1997.
- [8] B. E. A. Saleh and M. C. Teich, *Fundamentals of Photonics*. New York: John Wiley & Sons, 1991.
- [9] A. Yariv and P. Yeh, *Optical Waves in Crystals*. New York: John Wiley & Sons, 1984.
- [10] H. Nishihara, M. Haruna, and T. Suhara, *Optical Integrated Circuits*. New York: McGraw-Hill, 1989.
- [11] A. Yariv, “Coupled mode theory for guided-wave optics,” *IEEE J. Quantum Electron.*, vol. 9, pp. 919-933, 1973.
- [12] W. Warzanski, F. Heismann, and R. C. Alferness, “Polarization-independent electrooptically tunable narrow-band wavelength filter,” *Appl. Phys. Lett.*, vol. 53, pp. 13–15, July 1988.

- [13] H. F. Taylor, “Tunable spectral slicing filters for dense wavelength-division multiplexing,” *J. Lightwave Technol.*, vol. 21, pp. 837–847, 2003.
- [14] D. A. Smith, and J. J. Johnson, “Sidelobe suppression in an acoustooptic filter with a raised-cosine interaction strength,” *Appl. Phys. Lett.*, vol. 61, pp. 1025–1027, 1992.
- [15] I. R. Croston, A. D. Carr, N. J. Parsons, S. N. Radcliffe, and L. J. St. Ville, “Lithium niobate electro-optic tunable filter with high sidelobe suppression,” *Electron. Lett.*, vol. 29, pp. 157–159, 1993.
- [16] F. Heismann, and R. C. Alferness, “Wavelength-tunable electrooptic polarization conversion in birefringent waveguides,” *IEEE J. Quantum Electron.*, vol. 24, pp. 83–93, 1988.
- [17] H. F. Taylor and A. Yariv, “Guided Wave Optics,” *Proc. IEEE*, vol. 62, pp. 1044–1060, 1974.
- [18] P. Tang, O. Eknayan, and H. F. Taylor, “Rapidly tunable optical add-drop multiplexer (OADM) using a static-strain-induced grating in LiNbO₃,” *J. Lightwave Technol.*, vol. 21, pp. 236–245, 2003.

APPENDIX A

MATLAB CODE

Two_2_center.m

Description of Two_2_center.m

Two_2_center.m is a program that performs the matrix multiplication described in Chapter III to calculate the PCE of channel ± 2 in the structure for two sidebands. The refractive indices were obtained from modified Sellmeier equations [1] at the wavelength of 1.53 μm . The PCE of channel 0 and ± 1 is each obtained by adjusting the variable lambda_j and S.

Two_2_center.m Code

```

n3=2.2119;
n1=2.1386;
n=sqrt(n3*n1);
delta_ngr=0.08;

period=21;
lc=(179+3/4)*period;
lp=(20+1/4)*period;
L=lc*8+lp*7;

lambda0=period*(n3-n1);
lambdaJ=lambda0-0.0016;

npoints=2000;
S=pi/(2*1.51*10^4);

for int=1:npoints

    lambda = 1.37+0.0001*int;
    delta=2*pi*(n3-n1)*(1/lambda-1/lambda0);
    deltaJ=2*pi*delta_ngr*(1/lambdaJ-1/lambda0);
    d=delta/2;
    b1=2*pi/lambda*n1;
    b2=2*pi/lambda*n3;

    K1=S*cos(deltaJ*1/16*L);
    K1a=S*cos(deltaJ*1/16*L)*(1+0.5*cos(2*pi*(1/16-0.5)));
    ac1=cos(sqrt(K1^2+d^2)*lc)+i*d/sqrt(K1^2+d^2)*sin(sqrt(K1^2+d^2)*lc);
    bc1=-i*K1/sqrt(K1^2+d^2)*sin(sqrt(K1^2+d^2)*lc);
    ac1a=cos(sqrt(K1a^2+d^2)*lc)+i*d/sqrt(K1a^2+d^2)*sin(sqrt(K1a^2+d^2)*lc);
    bc1a=-i*K1a/sqrt(K1a^2+d^2)*sin(sqrt(K1a^2+d^2)*lc);

```

```

MC1=[ac1*exp(-i*(b1+d)*lc) bc1*exp(-i*(b1+d)*lc); -conj(bc1)*exp(-
i*(b2-d)*lc) conj(ac1)*exp(-i*(b2-d)*lc)];
MC1a=[ac1a*exp(-i*(b1+d)*lc) bc1a*exp(-i*(b1+d)*lc); -conj(bc1a)*exp(-
i*(b2-d)*lc) conj(ac1a)*exp(-i*(b2-d)*lc)];

MP=[exp(-i*b1*lp) 0; 0 exp(-i*b2*lp)];
K2=S*cos(deltaj*3/16*L);
K2a=S*cos(deltaj*3/16*L)*(1+0.5*cos(2*pi*(3/16-0.5)));
ac2=cos(sqrt(K2^2+d^2)*lc)+i*d/sqrt(K2^2+d^2)*sin(sqrt(K2^2+d^2)*lc);
bc2=-i*K2/sqrt(K2^2+d^2)*sin(sqrt(K2^2+d^2)*lc);
ac2a=cos(sqrt(K2a^2+d^2)*lc)+i*d/sqrt(K2a^2+d^2)*sin(sqrt(K2a^2+d^2)*l
c);
bc2a=-i*K2a/sqrt(K2a^2+d^2)*sin(sqrt(K2a^2+d^2)*lc);
MC2=[ac2*exp(-i*(b1+d)*lc) bc2*exp(-i*(b1+d)*lc); -conj(bc2)*exp(-
i*(b2-d)*lc) conj(ac2)*exp(-i*(b2-d)*lc)];
MC2a=[ac2a*exp(-i*(b1+d)*lc) bc2a*exp(-i*(b1+d)*lc); -conj(bc2a)*exp(-
i*(b2-d)*lc) conj(ac2a)*exp(-i*(b2-d)*lc)];
T2=MC2*MP;
T2a=MC2a*MP;

K3=S*cos(deltaj*5/16*L);
K3a=S*cos(deltaj*5/16*L)*(1+0.5*cos(2*pi*(5/16-0.5)));
ac3=cos(sqrt(K3^2+d^2)*lc)+i*d/sqrt(K3^2+d^2)*sin(sqrt(K3^2+d^2)*lc);
bc3=-i*K3/sqrt(K3^2+d^2)*sin(sqrt(K3^2+d^2)*lc);
ac3a=cos(sqrt(K3a^2+d^2)*lc)+i*d/sqrt(K3a^2+d^2)*sin(sqrt(K3a^2+d^2)*l
c);
bc3a=-i*K3a/sqrt(K3a^2+d^2)*sin(sqrt(K3a^2+d^2)*lc);
MC3=[ac3*exp(-i*(b1+d)*lc) bc3*exp(-i*(b1+d)*lc); -conj(bc3)*exp(-
i*(b2-d)*lc) conj(ac3)*exp(-i*(b2-d)*lc)];
MC3a=[ac3a*exp(-i*(b1+d)*lc) bc3a*exp(-i*(b1+d)*lc); -conj(bc3a)*exp(-
i*(b2-d)*lc) conj(ac3a)*exp(-i*(b2-d)*lc)];
T3=MC3*MP;
T3a=MC3a*MP;

K4=S*cos(deltaj*7/16*L);
K4a=S*cos(deltaj*7/16*L)*(1+0.5*cos(2*pi*(7/16-0.5)));
ac4=cos(sqrt(K4^2+d^2)*lc)+i*d/sqrt(K4^2+d^2)*sin(sqrt(K4^2+d^2)*lc);
bc4=-i*K4/sqrt(K4^2+d^2)*sin(sqrt(K4^2+d^2)*lc);
ac4a=cos(sqrt(K4a^2+d^2)*lc)+i*d/sqrt(K4a^2+d^2)*sin(sqrt(K4a^2+d^2)*l
c);
bc4a=-i*K4a/sqrt(K4a^2+d^2)*sin(sqrt(K4a^2+d^2)*lc);
MC4=[ac4*exp(-i*(b1+d)*lc) bc4*exp(-i*(b1+d)*lc); -conj(bc4)*exp(-
i*(b2-d)*lc) conj(ac4)*exp(-i*(b2-d)*lc)];
MC4a=[ac4a*exp(-i*(b1+d)*lc) bc4a*exp(-i*(b1+d)*lc); -conj(bc4a)*exp(-
i*(b2-d)*lc) conj(ac4a)*exp(-i*(b2-d)*lc)];
T4=MC4*MP;
T4a=MC4a*MP;

K5=S*cos(deltaj*9/16*L);
K5a=S*cos(deltaj*9/16*L)*(1+0.5*cos(2*pi*(9/16-0.5)));
ac5=cos(sqrt(K5^2+d^2)*lc)+i*d/sqrt(K5^2+d^2)*sin(sqrt(K5^2+d^2)*lc);
bc5=-i*K5/sqrt(K5^2+d^2)*sin(sqrt(K5^2+d^2)*lc);
ac5a=cos(sqrt(K5a^2+d^2)*lc)+i*d/sqrt(K5a^2+d^2)*sin(sqrt(K5a^2+d^2)*l
c);
bc5a=-i*K5a/sqrt(K5a^2+d^2)*sin(sqrt(K5a^2+d^2)*lc);
MC5=[ac5*exp(-i*(b1+d)*lc) bc5*exp(-i*(b1+d)*lc); -conj(bc5)*exp(-
i*(b2-d)*lc) conj(ac5)*exp(-i*(b2-d)*lc)];
MC5a=[ac5a*exp(-i*(b1+d)*lc) bc5a*exp(-i*(b1+d)*lc); -conj(bc5a)*exp(-
i*(b2-d)*lc) conj(ac5a)*exp(-i*(b2-d)*lc)];
T5=MC5*MP;
T5a=MC5a*MP;

K6=S*cos(deltaj*11/16*L);

```

```

K6a=S*cos(deltaj*11/16*L)*(1+0.5*cos(2*pi*(11/16-0.5)));
ac6=cos(sqrt(K6^2+d^2)*lc)+i*d/sqrt(K6^2+d^2)*sin(sqrt(K6^2+d^2)*lc);
bc6=-i*K6/sqrt(K6^2+d^2)*sin(sqrt(K6^2+d^2)*lc);
ac6a=cos(sqrt(K6a^2+d^2)*lc)+i*d/sqrt(K6a^2+d^2)*sin(sqrt(K6a^2+d^2)*lc);
bc6a=-i*K6a/sqrt(K6a^2+d^2)*sin(sqrt(K6a^2+d^2)*lc);
MC6=[ac6*exp(-i*(b1+d)*lc) bc6*exp(-i*(b1+d)*lc); -conj(bc6)*exp(-i*(b2-d)*lc) conj(ac6)*exp(-i*(b2-d)*lc)];
MC6a=[ac6a*exp(-i*(b1+d)*lc) bc6a*exp(-i*(b1+d)*lc); -conj(bc6a)*exp(-i*(b2-d)*lc) conj(ac6a)*exp(-i*(b2-d)*lc)];
T6=MC6*MP;
T6a=MC6a*MP;

K7=S*cos(deltaj*13/16*L);
K7a=S*cos(deltaj*13/16*L)*(1+0.5*cos(2*pi*(13/16-0.5)));
ac7=cos(sqrt(K7^2+d^2)*lc)+i*d/sqrt(K7^2+d^2)*sin(sqrt(K7^2+d^2)*lc);
bc7=-i*K7/sqrt(K7^2+d^2)*sin(sqrt(K7^2+d^2)*lc);
ac7a=cos(sqrt(K7a^2+d^2)*lc)+i*d/sqrt(K7a^2+d^2)*sin(sqrt(K7a^2+d^2)*lc);
bc7a=-i*K7a/sqrt(K7a^2+d^2)*sin(sqrt(K7a^2+d^2)*lc);
MC7=[ac7*exp(-i*(b1+d)*lc) bc7*exp(-i*(b1+d)*lc); -conj(bc7)*exp(-i*(b2-d)*lc) conj(ac7)*exp(-i*(b2-d)*lc)];
MC7a=[ac7a*exp(-i*(b1+d)*lc) bc7a*exp(-i*(b1+d)*lc); -conj(bc7a)*exp(-i*(b2-d)*lc) conj(ac7a)*exp(-i*(b2-d)*lc)];
T7=MC7*MP;
T7a=MC7a*MP;

K8=S*cos(deltaj*15/16*L);
K8a=S*cos(deltaj*15/16*L)*(1+0.5*cos(2*pi*(15/16-0.5)));
ac8=cos(sqrt(K8^2+d^2)*lc)+i*d/sqrt(K8^2+d^2)*sin(sqrt(K8^2+d^2)*lc);
bc8=-i*K8/sqrt(K8^2+d^2)*sin(sqrt(K8^2+d^2)*lc);
ac8a=cos(sqrt(K8a^2+d^2)*lc)+i*d/sqrt(K8a^2+d^2)*sin(sqrt(K8a^2+d^2)*lc);
bc8a=-i*K8a/sqrt(K8a^2+d^2)*sin(sqrt(K8a^2+d^2)*lc);
MC8=[ac8*exp(-i*(b1+d)*lc) bc8*exp(-i*(b1+d)*lc); -conj(bc8)*exp(-i*(b2-d)*lc) conj(ac8)*exp(-i*(b2-d)*lc)];
MC8a=[ac8a*exp(-i*(b1+d)*lc) bc8a*exp(-i*(b1+d)*lc); -conj(bc8a)*exp(-i*(b2-d)*lc) conj(ac8a)*exp(-i*(b2-d)*lc)];
T8=MC8*MP;
T8a=MC8a*MP;

C=T8*T7*T6*T5*T4*T3*T2*MC1;
PCE(int)=10*log10((abs(C(1,2)))^2);
Ca=T8a*T7a*T6a*T5a*T4a*T3a*T2a*MC1a;
PCEa(int)=10*log10((abs(Ca(1,2)))^2);

dvec(int)=delta;
end;

plot(dvec*L, PCE, ':k');
hold on
plot(dvec*L, PCEa, 'k');
hold on
plot(dvec*L,-3, 'k', dvec*L,-10, 'k', dvec*L,-20, 'k');
hold off
set(gcf,'Color','white');
xlabel('\Delta L');
ylabel('PCE(dB)');
xlim([-30,30]);
ylim([-30,0]);

```

Single_2_center.m

Description of Single_2_center.m

Single_2_center.m was written to calculate the PCE of channel 2 in the modified configuration for single sideband. In the similar manner to channel selection for two sidebands, the PCE of selectable channel is achieved by changing the value of variable lambda_j and S.

Signle_2_center.m Code

```

n3=2.2119;
n1=2.1386;
n=sqrt(n3*n1);
delta_ngr=0.08;

period=21;
lc=(179+3/4)*period;
lpa=(20)*period;
lpb=(20+2/4)*period;
L=lc*8+lpa*4+lpb*3;

lambda0=period*(n3-n1);
lambda_j=lambda0-0.0016;

npoints=2000;

S=pi/(2*3.02*10^4);

for int=1:npoints

lambda = 1.37+0.0001*int;
delta=2*pi*(n3-n1)*(1/lambda-1/lambda0);
delta_j=2*pi*delta_ngr*(1/lambda_j-1/lambda0);
d=delta/2;
b1=2*pi/lambda*n1;
b2=2*pi/lambda*n3;

K1=S*cos(delta_j*1/16*L);
K1a=S*cos(delta_j*1/16*L)*(1+0.5*cos(2*pi*(1/16-0.5)));
ac1=cos(sqrt(K1^2+d^2)*lc)+i*d/sqrt(K1^2+d^2)*sin(sqrt(K1^2+d^2)*lc);
bc1=-i*K1/sqrt(K1^2+d^2)*sin(sqrt(K1^2+d^2)*lc);
ac1a=cos(sqrt(K1a^2+d^2)*lc)+i*d/sqrt(K1a^2+d^2)*sin(sqrt(K1a^2+d^2)*lc);
bc1a=-i*K1a/sqrt(K1a^2+d^2)*sin(sqrt(K1a^2+d^2)*lc);
MC1=[ac1*exp(-i*(b1+d)*lc) bc1*exp(-i*(b1+d)*lc); -conj(bc1)*exp(-i*(b2-d)*lc) conj(ac1)*exp(-i*(b2-d)*lc)];
MC1a=[ac1a*exp(-i*(b1+d)*lc) bc1a*exp(-i*(b1+d)*lc); -conj(bc1a)*exp(-i*(b2-d)*lc) conj(ac1a)*exp(-i*(b2-d)*lc)];

MP2=[exp(-i*b1*lpa) 0; 0 exp(-i*b2*lpa)];
K2=S*sin(delta_j*3/16*L);
K2a=S*sin(delta_j*3/16*L)*(1+0.5*cos(2*pi*(3/16-0.5)));
ac2=cos(sqrt(K2^2+d^2)*lc)+i*d/sqrt(K2^2+d^2)*sin(sqrt(K2^2+d^2)*lc);
bc2=-i*K2/sqrt(K2^2+d^2)*sin(sqrt(K2^2+d^2)*lc);
ac2a=cos(sqrt(K2a^2+d^2)*lc)+i*d/sqrt(K2a^2+d^2)*sin(sqrt(K2a^2+d^2)*lc);

```

```

bc2a=-i*K2a/sqrt(K2a^2+d^2)*sin(sqrt(K2a^2+d^2)*lc);
MC2=[ac2*exp(-i*(b1+d)*lc) bc2*exp(-i*(b1+d)*lc); -conj(bc2)*exp(-
i*(b2-d)*lc) conj(ac2)*exp(-i*(b2-d)*lc)];
MC2a=[ac2a*exp(-i*(b1+d)*lc) bc2a*exp(-i*(b1+d)*lc); -conj(bc2a)*exp(-
i*(b2-d)*lc) conj(ac2a)*exp(-i*(b2-d)*lc)];
T2=MC2*MP2;
T2a=MC2a*MP2;

MP3=[exp(-i*b1*lpb) 0; 0 exp(-i*b2*lpb)];
K3=S*cos(deltaj*5/16*L);
K3a=S*cos(deltaj*5/16*L)*(1+0.5*cos(2*pi*(5/16-0.5)));
ac3=cos(sqrt(K3^2+d^2)*lc)+i*d/sqrt(K3^2+d^2)*sin(sqrt(K3^2+d^2)*lc);
bc3=-i*K3/sqrt(K3^2+d^2)*sin(sqrt(K3^2+d^2)*lc);
ac3a=cos(sqrt(K3a^2+d^2)*lc)+i*d/sqrt(K3a^2+d^2)*sin(sqrt(K3a^2+d^2)*l
c);
bc3a=-i*K3a/sqrt(K3a^2+d^2)*sin(sqrt(K3a^2+d^2)*lc);
MC3=[ac3*exp(-i*(b1+d)*lc) bc3*exp(-i*(b1+d)*lc); -conj(bc3)*exp(-
i*(b2-d)*lc) conj(ac3)*exp(-i*(b2-d)*lc)];
MC3a=[ac3a*exp(-i*(b1+d)*lc) bc3a*exp(-i*(b1+d)*lc); -conj(bc3a)*exp(-
i*(b2-d)*lc) conj(ac3a)*exp(-i*(b2-d)*lc)];
T3=MC3*MP3;
T3a=MC3a*MP3;

MP4=[exp(-i*b1*lpa) 0; 0 exp(-i*b2*lpa)];
K4=S*sin(deltaj*7/16*L);
K4a=S*sin(deltaj*7/16*L)*(1+0.5*cos(2*pi*(7/16-0.5)));
ac4=cos(sqrt(K4^2+d^2)*lc)+i*d/sqrt(K4^2+d^2)*sin(sqrt(K4^2+d^2)*lc);
bc4=-i*K4/sqrt(K4^2+d^2)*sin(sqrt(K4^2+d^2)*lc);
ac4a=cos(sqrt(K4a^2+d^2)*lc)+i*d/sqrt(K4a^2+d^2)*sin(sqrt(K4a^2+d^2)*l
c);
bc4a=-i*K4a/sqrt(K4a^2+d^2)*sin(sqrt(K4a^2+d^2)*lc);
MC4=[ac4*exp(-i*(b1+d)*lc) bc4*exp(-i*(b1+d)*lc); -conj(bc4)*exp(-
i*(b2-d)*lc) conj(ac4)*exp(-i*(b2-d)*lc)];
MC4a=[ac4a*exp(-i*(b1+d)*lc) bc4a*exp(-i*(b1+d)*lc); -conj(bc4a)*exp(-
i*(b2-d)*lc) conj(ac4a)*exp(-i*(b2-d)*lc)];
T4=MC4*MP4;
T4a=MC4a*MP4;

MP5=[exp(-i*b1*lpb) 0; 0 exp(-i*b2*lpb)];
K5=S*cos(deltaj*9/16*L);
K5a=S*cos(deltaj*9/16*L)*(1+0.5*cos(2*pi*(9/16-0.5)));
ac5=cos(sqrt(K5^2+d^2)*lc)+i*d/sqrt(K5^2+d^2)*sin(sqrt(K5^2+d^2)*lc);
bc5=-i*K5/sqrt(K5^2+d^2)*sin(sqrt(K5^2+d^2)*lc);
ac5a=cos(sqrt(K5a^2+d^2)*lc)+i*d/sqrt(K5a^2+d^2)*sin(sqrt(K5a^2+d^2)*l
c);
bc5a=-i*K5a/sqrt(K5a^2+d^2)*sin(sqrt(K5a^2+d^2)*lc);
MC5=[ac5*exp(-i*(b1+d)*lc) bc5*exp(-i*(b1+d)*lc); -conj(bc5)*exp(-
i*(b2-d)*lc) conj(ac5)*exp(-i*(b2-d)*lc)];
MC5a=[ac5a*exp(-i*(b1+d)*lc) bc5a*exp(-i*(b1+d)*lc); -conj(bc5a)*exp(-
i*(b2-d)*lc) conj(ac5a)*exp(-i*(b2-d)*lc)];
T5=MC5*MP5;
T5a=MC5a*MP5;

MP6=[exp(-i*b1*lpa) 0; 0 exp(-i*b2*lpa)];
K6=S*sin(deltaj*11/16*L);
K6a=S*sin(deltaj*11/16*L)*(1+0.5*cos(2*pi*(11/16-0.5)));
ac6=cos(sqrt(K6^2+d^2)*lc)+i*d/sqrt(K6^2+d^2)*sin(sqrt(K6^2+d^2)*lc);
bc6=-i*K6/sqrt(K6^2+d^2)*sin(sqrt(K6^2+d^2)*lc);
ac6a=cos(sqrt(K6a^2+d^2)*lc)+i*d/sqrt(K6a^2+d^2)*sin(sqrt(K6a^2+d^2)*l
c);
bc6a=-i*K6a/sqrt(K6a^2+d^2)*sin(sqrt(K6a^2+d^2)*lc);
MC6=[ac6*exp(-i*(b1+d)*lc) bc6*exp(-i*(b1+d)*lc); -conj(bc6)*exp(-
i*(b2-d)*lc) conj(ac6)*exp(-i*(b2-d)*lc)];

```

```

MC6a=[ac6a*exp(-i*(b1+d)*lc) bc6a*exp(-i*(b1+d)*lc); -conj(bc6a)*exp(-
i*(b2-d)*lc) conj(ac6a)*exp(-i*(b2-d)*lc)];
T6=MC6*MP6;
T6a=MC6a*MP6;

MP7=[exp(-i*b1*lpb) 0; 0 exp(-i*b2*lpb)];
K7=S*cos(deltaj*13/16*L);
K7a=S*cos(deltaj*13/16*L)*(1+0.5*cos(2*pi*(13/16-0.5)));
ac7=cos(sqrt(K7^2+d^2)*lc)+i*d/sqrt(K7^2+d^2)*sin(sqrt(K7^2+d^2)*lc);
bc7=-i*K7/sqrt(K7^2+d^2)*sin(sqrt(K7^2+d^2)*lc);
ac7a=cos(sqrt(K7a^2+d^2)*lc)+i*d/sqrt(K7a^2+d^2)*sin(sqrt(K7a^2+d^2)*l
c);
bc7a=-i*K7a/sqrt(K7a^2+d^2)*sin(sqrt(K7a^2+d^2)*lc);
MC7=[ac7*exp(-i*(b1+d)*lc) bc7*exp(-i*(b1+d)*lc); -conj(bc7)*exp(-
i*(b2-d)*lc) conj(ac7)*exp(-i*(b2-d)*lc)];
MC7a=[ac7a*exp(-i*(b1+d)*lc) bc7a*exp(-i*(b1+d)*lc); -conj(bc7a)*exp(-
i*(b2-d)*lc) conj(ac7a)*exp(-i*(b2-d)*lc)];
T7=MC7*MP7;
T7a=MC7a*MP7;

MP8=[exp(-i*b1*lpa) 0; 0 exp(-i*b2*lpa)];
K8=S*sin(deltaj*15/16*L);
K8a=S*sin(deltaj*15/16*L)*(1+0.5*cos(2*pi*(15/16-0.5)));
ac8=cos(sqrt(K8^2+d^2)*lc)+i*d/sqrt(K8^2+d^2)*sin(sqrt(K8^2+d^2)*lc);
bc8=-i*K8/sqrt(K8^2+d^2)*sin(sqrt(K8^2+d^2)*lc);
ac8a=cos(sqrt(K8a^2+d^2)*lc)+i*d/sqrt(K8a^2+d^2)*sin(sqrt(K8a^2+d^2)*l
c);
bc8a=-i*K8a/sqrt(K8a^2+d^2)*sin(sqrt(K8a^2+d^2)*lc);
MC8=[ac8*exp(-i*(b1+d)*lc) bc8*exp(-i*(b1+d)*lc); -conj(bc8)*exp(-
i*(b2-d)*lc) conj(ac8)*exp(-i*(b2-d)*lc)];
MC8a=[ac8a*exp(-i*(b1+d)*lc) bc8a*exp(-i*(b1+d)*lc); -conj(bc8a)*exp(-
i*(b2-d)*lc) conj(ac8a)*exp(-i*(b2-d)*lc)];
T8=MC8*MP8;
T8a=MC8a*MP8;

C=T8*T7*T6*T5*T4*T3*T2*MC1;
PCE(int)=10*log10((abs(C(1,2)))^2);
Ca=T8a*T7a*T6a*T5a*T4a*T3a*T2a*MC1a;
PCEa(int)=10*log10((abs(Ca(1,2)))^2);

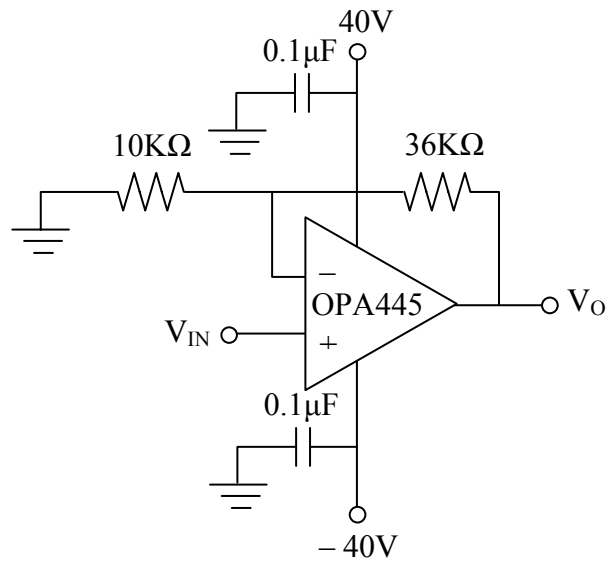
dvec(int)=delta;
end;

plot(dvec*L, PCE, ':k');
hold on
plot(dvec*L, PCEa, 'k');
hold on
plot(dvec*L,-3, 'k', dvec*L,-10, 'k', dvec*L,-20, 'k');
hold off
set(gcf,'Color','white');
xlabel('\Delta L');
ylabel('PCE(dB)');
xlim([-30,30]);
ylim([-30,0]);

```

REFERENCES FOR APPENDIX A

- [1] S. D. Smith, H. D. Riccius, and R. P. Edwin, *Opt.Comm.*, vol. 17, pp. 332–335, 1976 and vol. 20, p. 188, 1977.

APPENDIX B**OP-AMP CIRCUIT**

VITA

Changdong Kim was born in Yecheon, Korea. He received the B.S. degree in electrical engineering from Korea University, Seoul, Korea in August 2000. From 2000 to 2003, he was with Samsung Electronics, Suwon, Korea, where he was an engineer of the Optical Communication Lab. He began his graduate study at Texas A&M University in August 2003 and received his M.S. degree in Dept. of Electrical Engineering.

Mailing Address: 214 Zachry Engineering Center
TAMU 3128
College Station, TX 77843

The typist for this thesis was Changdong Kim.